NASA/TM—2004-213221

Probing Within the Boundary Layer of an Airfoil by Using the Wind Numerical Code

Richard H. Cavicchi
Glenn Research Center, Cleveland, Ohio

September 2004

The NASA STI Program Office . . . in Profile

Since its founding, NASA has been dedicated to the advancement of aeronautics and space science. The NASA Scientific and Technical Information (STI) Program Office plays a key part in helping NASA maintain this important role.

The NASA STI Program Office is operated by Langley Research Center, the Lead Center for NASA's scientific and technical information. The NASA STI Program Office provides access to the NASA STI Database, the largest collection of aeronautical and space science STI in the world. The Program Office is also NASA's institutional mechanism for disseminating the results of its research and development activities. These results are published by NASA in the NASA STI Report Series, which includes the following report types:

- TECHNICAL PUBLICATION. Reports of completed research or a major significant phase of research that present the results of NASA programs and include extensive data or theoretical analysis. Includes compilations of significant scientific and technical data and information deemed to be of continuing reference value. NASA's counterpart of peer-reviewed formal professional papers but has less stringent limitations on manuscript length and extent of graphic presentations.

- TECHNICAL MEMORANDUM. Scientific and technical findings that are preliminary or of specialized interest, e.g., quick release reports, working papers, and bibliographies that contain minimal annotation. Does not contain extensive analysis.

- CONTRACTOR REPORT. Scientific and technical findings by NASA-sponsored contractors and grantees.

- CONFERENCE PUBLICATION. Collected papers from scientific and technical conferences, symposia, seminars, or other meetings sponsored or cosponsored by NASA.

- SPECIAL PUBLICATION. Scientific, technical, or historical information from NASA programs, projects, and missions, often concerned with subjects having substantial public interest.

- TECHNICAL TRANSLATION. English-language translations of foreign scientific and technical material pertinent to NASA's mission.

Specialized services that complement the STI Program Office's diverse offerings include creating custom thesauri, building customized databases, organizing and publishing research results . . . even providing videos.

For more information about the NASA STI Program Office, see the following:

- Access the NASA STI Program Home Page at ***http://www.sti.nasa.gov***

- E-mail your question via the Internet to help@sti.nasa.gov

- Fax your question to the NASA Access Help Desk at 301–621–0134

- Telephone the NASA Access Help Desk at 301–621–0390

- Write to:
  NASA Access Help Desk
  NASA Center for AeroSpace Information
  7121 Standard Drive
  Hanover, MD 21076

NASA/TM—2004-213221

Probing Within the Boundary Layer of an Airfoil by Using the Wind Numerical Code

Richard H. Cavicchi
Glenn Research Center, Cleveland, Ohio

National Aeronautics and
Space Administration

Glenn Research Center

September 2004

This work was sponsored by the Low Emissions Alternative Power Project of the Vehicle Systems Program at the NASA Glenn Research Center.

Available from

NASA Center for Aerospace Information
7121 Standard Drive
Hanover, MD 21076

National Technical Information Service
5285 Port Royal Road
Springfield, VA 22100

Available electronically at http://gltrs.grc.nasa.gov

Probing Within the Boundary Layer of an Airfoil by Using the Wind Numerical Code

Richard H. Cavicchi
National Aeronautics and Space Administration
Glenn Research Center
Cleveland, Ohio 44135

Abstract

A detailed boundary layer investigation of an NACA 0012 airfoil was made by applying the WIND code at the NASA Glenn Research Center. Structured C-grids of selected configurations were fitted around the airfoil. Grids with dense spacing to capture the boundary layer provided for obtaining accurate results in this region. Concurrent with the boundary layer investigation, contour plots of overall performance of the airfoil were also obtained. A Mach number of 0.80, a Reynolds number of 4,000,000, and a zero angle of attack were set to correspond with numerical and experimental investigations reported in the literature, for comparison with the overall performance. The results were favorable for both the boundary layer investigations and the performance. As WIND evolves, it is intended to run WIND using unstructured grids to compare such results with the current structured grid results.

Introduction

At the National Aeronautics and Space Administration (NASA) Glenn Research Center, the WIND code has been applied to a National Advisory Committee for Aeronautics (NACA) 0012 airfoil in turbulent transonic flow. The WIND code numerically solves the Navier-Stokes equations of fluid mechanics, and incorporates a provision for turbulence modeling. WIND is described in full detail in reference 1. The NACA 0012 airfoil is the widely accepted mainstay of the NACA four-digit series of airfoils.

Selected two-dimensional structured C-grids designed by the author and generated by a program written by him, were applied to the airfoil. The grids are of various densities. The primary purpose of this report is to investigate aerodynamic conditions within the boundary layer on the airfoil. In the course of the computations the overall performance of the airfoil was also obtained. This performance will be compared with that available in the literature. Both numerical and experimental references were used. The secondary purpose of the current effort is to provide a basis for comparison of WIND results using structured grids to assess WIND's subsequent capability using unstructured grids. Thus, this investigation sets up this basis.

In the current calculations, a freestream Mach number of 0.80 was used, such that Mach 1.0 is achieved and a shockwave occurs on the airfoil. A Reynolds number of 4,000,000 and a zero angle of attack were used to match the literature conditions. Thus, the current investigation will display the capability of WIND to define the shock wave, although the grids themselves play a prominent role. All WIND calculations performed in this investigation assumed a viscous wall boundary condition, except for one run made for an inviscid wall comparison. The Spalart-Allmaras turbulence model was used in all the calculations. Plots from the WIND results were made by using PLOT3D (ref. 2), CFPOST (ref. 1) and PLOTC (ref. 3). All the calculations were made on a Silicon Graphics Incorporated (SGI) machine.

Symbols

a	Speed of sound, ft/sec
a_0, a_1, a_2, a_3, a_4	Constants in equation (1)
c	Chord of airfoil, ft
C_p	Coefficient of pressure, $\dfrac{p - p_\infty}{0.5\rho_\infty V_\infty^2}$
i,j	Grid indices
M	Mach number
p	Static pressure, psi
P_0	Stagnation pressure, psi
$\dfrac{P_{T2}}{P_{T1}}$	Stagnation pressure ratio across shock wave
R	Maximum upstream grid radius, ft
t	Maximum thickness of airfoil, as a decimal
u	Axial component of velocity, ft/sec
V	Velocity magnitude, ft/sec
x,y	Cartesian coordinates, ft
xL	Downstream length, ft
yH	Grid height, ft
α	Angle of attack, degrees
γ	Ratio of specific heats
ρ	Density, lb/ft^3

Subscripts

∞	Freestream conditions
1	Conditions just upstream of shock wave

The Airfoil

In the 1930's NACA designed a family of airfoils, all of which were spawn from the same equation. The father of this equation is shown here as

$$\pm y = a_0x^{.5} - a_1x - a_2x^2 + a_3x^3 - a_4x^4 \tag{1}$$

This equation and its subsequent discussion were taken from reference (4). The chord c for the airfoils represented by equation (1) was set at 1.0 foot. The constants a_0 to a_4 were evaluated by setting constraints so that equation (1) would yield a shape that had proved to be efficient in previous experiments. With these evaluations, equation (1) takes the form of equation (2).

$$\pm y = 0.2969x^{.5} - 0.126x - 0.3516x^2 + 0.2843x^3 - 0.1015x^4 \tag{2}$$

This equation defines the "basic section".

Reference 4 takes the basic section a step further by introducing the maximum airfoil thickness t into equation (2). This step yields equation (3).

$$\pm y = 5t(0.2969x^{.5} - 0.126\,x - 0.3516\,x^2 + 0.2843\,x^3 - 0.1015\,x^4) \qquad (3)$$

Thus, equation (3) establishes the NACA 4-digit wing sections. The shapes of these airfoils, along with their coordinates and performances, are presented in reference 5.

Note that when the maximum airfoil thickness t is 0.20 in equation (3), equation (2) results. However, for the NACA 0012 airfoil the value of t is 0.12. Figure 1, taken from reference 5, presents the NACA 0012 profile together with its coordinates, which were used herein. Figure 1 also displays the axial distribution of the square of the velocity V on the profile, which will be discussed subsequently. As in figure 1, the chord of the airfoil c used herein is 1.0 foot.

The Grids

Two-dimensional structured C-grids designed by the author and that were programmed and run by him on a SGI computer were fitted around the airfoil of figure 1. Each grid was constructed as a single block. A set of indices (i,j) denotes the radial and lateral lines, respectively, that connect the points in the field around the profile.

The following table presents the extent of the grids. Figure 2(a) describes these dimensions.

Grid Upstream Radius	Grid Height	Grid Downstream Length
$R/c = 4$	$yH/c = 4$	$xL/c = 5$
2	$yH/c = 2$	"
1	$yH/c = 1$	"

Maximum values used in the calculations for the indices (i,j) are tabulated below.

	imax	jmax
Cases 1 to 4	73	30, 60, 120, 960
Cases 5 to 8	113	30, 60, 120, 960

Constant grid spacing in the j-direction rather than clustering was used to provide the ability to prescribe a given number of grid lines within the boundary layer.

Figure 2(a) shows the 113 x 120 grid. Arbitrarily, the i-index, for radial lines, begins with i = 1 at the lower half of the grid at the downstream exit (the lower right in figure 2(a)). The lines of constant i then progress upstream under the airfoil, around the nose, above the profile, and downstream to the exit, where i = imax.

The count for the j-index, for lateral lines, begins at j = 1 on the airfoil outline. The lines of constant j wrap around the airfoil as shown in figure 2(a) to where the count reaches $j$max at the outermost lateral line. The j-index spacing for the 113 x 120 grid is 0.03361c. For the 113 x 960 grid, it is 0.00417c.

Figure 2(b) displays the 113 x 960 grid in the vicinity of the profile. Figure 2(c) shows the approximate boundary layer, using this grid, in relation to the first 8 grid lateral lines (j = 2 to 9). The boundary layer curve in figure 2(c) will be discussed subsequently.

Input

The following initial freestream conditions were specified for the runs using WIND.

Mach number	0.80
Static pressure	7.226 psi.
Stagnation temperature	393.87 °R
Reynolds number	4,000,000
Angle of attack	0 deg

The Reynolds number is that used to enable the literature comparisons. The Spalart-Allmaras turbulence model was used throughout this investigation.

Boundary Conditions

The boundary conditions are displayed concisely in figure 3. This is a grid management (GMAN) file used in pre-processing for WIND. A viscous wall (no slip) condition was specified on the airfoil profile. For comparison, one run was made assuming an inviscid wall (slip).

Results and Discussion

Most of the following discussions pertain to results using the most dense grid, 113 x 960. Comparisons will be made with: no downstream grid, an inviscid wall, coarser grids, shorter grid heights, and the available literature. In the contour plots, pressure and velocity are non-dimensionalized by standard PLOT3D procedures shown in reference 2.

Convergence

History of residuals.—Figure 4 presents the residual history of the Navier-Stokes equations through 2000 iterations. Complete termination of WIND occurred after 12,050.70 seconds of CPU time. Figure 4 shows that the calculations essentially converged during this run.

Drag and lift coefficients.—Setting zero angle of attack yields no lift, but it does not eliminate the drag on the airfoil. Figure 5(a) presents the drag coefficient as a function of iteration. The calculated drag decreased to a stable value after about 900 iterations.

The companion plot, for lift, appears in figure 5(b). This figure displays a wild variation of lift during the iteration process. However, the gyrations are near and about the nominal value of zero as a consequence of the zero angle of attack. Thus, the magnitudes of the gyrations are actually very small, the maximum value being only about 0.0014.

Overall Performance

Flow field contours.—Flow field contours are presented in figures 6(a) to 6(d) for Mach number, static pressure, stagnation pressure, and axial component of velocity, respectively. The PLOT3D graphics method was used for these presentations. The most outstanding feature in figure 6 is the shock wave that appears about midway along the airfoil. This occurrence stands out most vividly in figure 6(b) where the static pressure contour lines are packed very closely. Note that Mach 1.0 is achieved at about 20 percent of the chord length from the nose.

The stagnation pressure across a shock wave decreases because the process is not isentropic. Reference 6 gives the stagnation pressure ratio across a shock wave as

$$P_{T2}/P_{T1} = \left((\gamma+1)M_1^2/\left((\gamma-1)M_1^2+2\right)\right)^{\frac{\gamma}{\gamma-1}} \left((\gamma+1)/\left(2M_1^2-(\gamma-1)\right)\right)^{\frac{\gamma}{\gamma-1}} \tag{4}$$

For the maximum Mach number shown in figure 6(a) of 1.25, equation (4) gives a ratio of 0.98706 for $\frac{P_{T2}}{P_{T1}}$. The contour plot of stagnation pressure also shows dramatically the location of the shock wave in figure 6(c).

The axial component of velocity u presented in the contour plot of figure 6(d) is positive throughout the region. No negative values for u near the airfoil suggests that separation does not occur. NACA 0012 was designed to avoid such an occurrence.

Investigation Within the Boundary Layer

The figures in the following discussions will be used to explore the aerodynamic variables in the region of flow within the boundary layer, that is depicted in figure 2(c). Most of the figures were produced by using CFPOST.

Coefficient of pressure.—Figure 7 presents the axial variation of the coefficient of pressure C_p on the airfoil (at $j = 1$). This variable is negative for pressures less than freestream pressure, which occurs over the airfoil. Consequently, the negative of C_p is commonly plotted for airfoils. Because the angle of attack used in this investigation is zero, C_p for both the upper and lower profile outlines is the same. If an angle of attack had been used, the curve for C_p for the lower profile would lie beneath the curve shown in figure 7. The area between the two curves would have represented the lift. Hence, figure 5(b) would have shown positive values for the lift. Figure 7 will be used as a standard for comparison with other cases for C_p in this investigation.

The abscissa in figure 7 runs from 0 to 1 foot, which is the chord length. The steep negative slope of $-C_p$ in figure 7 at about $x = 0.4$ foot displays the sharp rise in static pressure across the shock wave. Its location was previously noted in the discussion of stagnation pressure contours in figure 6(c).

Variation of axial velocity with y.—The variation of the axial component of velocity u with the ordinate y is presented in figure 8 for the region above the profile. Figures 8(a) and 8(b) depict the fore part of the region. Curves of constant index i are shown from $i = 58$ to $i = 66$. The curves in figure 8(a) were made for values of index j from $j = 2$ to $j = 100$. The curves in figure 8(b) represent $j = 2$ to $j = 20$ to define the boundary layer. Figures 8(c) and 8(d) show the variations in u for $i = 67$ to $i = 74$. In figure 8, 2 is the lowest value used for j because $j = 1$ is the profile itself, on which the velocity is zero because of the viscous wall assumption.

The upward turns in the curves for u in figures 8(b) and 8(d) were used to estimate the boundary layer thicknesses shown in figure 2(c). There is no evidence of separation in figure 8.

Axial variation of Mach number.—The axial variation of Mach number M is presented in figure 9 for selected values of j from 2 to 50. Figure 9(a) presents M in which x extends from 0 to 1 foot; whereas the entire range of x is presented in figure 9(b). The shapes of the curves for M in figure 9(a) closely resemble those for C_p in figure 7. The curves in figure 9 reach a maximum of about 1.25 at an axial location of about 30 percent of chord length. Then the Mach number decreases down to 0.8 and below within the wake region. No indication of a downstream vortex appears in figure 9(b).

Axial variation of static pressure.—The axial variation of static pressure p for selected values of index j from j = 1 to j = 50 are presented in figure 10. Pressure does exist on the profile, so a curve for j = 1 is shown. Figures 9 and 10 are essentially upside down images of each other. This correspondence occurs because pressure drives the velocity. Thus, the steep decline of Mach number at x = 0.4 in figure 9 is a result of the shock wave that occurs. The slopes of the pressure curves there decrease with distance away from the airfoil (higher values of j).

Axial variation of stagnation pressure.—Figure 11(a) presents the axial variation of stagnation pressure P_0. Again, j varies from 1 to 50. From the nose (x = 0) figure 11(a) shows that for j = 1 the stagnation pressure drops steeply to a very low value on the profile at the shock wave. At j = 2, P_0 also drops sharply at the nose, but to nowhere as low a value. It was shown by equation (4) that stagnation pressure decreases across a shock wave. In figure 11(a) at x = 0.4 the decrease is just a ripple for j = 3. But on the profile itself (j = 1), P_0 rises significantly in response to the freestream impressing itself on the airfoil flowfield.

Effect of No Downstream Grid

Contour plots.—Figures 12(a) to 12(c) present contour plots of M, p, and u resulting from omitting the downstream grid. The primary difference between the plots in figure 12 and their counterparts in figure 6 (with a downstream grid) is that the shock wave is predicted to occur farther downstream when the downstream grid is omitted. This result is a function of the downstream boundary condition assumption.

Coefficient of pressure.—Figure 13 compares the coefficient of pressure for the case with no downstream grid with that for the full 113 x 960 grid of figure 7. Figure 13 shows with great clarity that having no downstream grid results in predicting the shock wave location farther downstream than the full grid. Figure 13 also predicts the shock wave as beginning 0.2 foot farther downstream as well as steeper in slope. Notice that the two curves in figure 13 are identical upstream of the shock wave because the grids are the same there. This fact demonstrates the well known phenomenon that downstream effects can not propagate upstream through supersonic flow (which immediately precedes the shock wave). However, the effects with or without a downstream grid do propagate upstream in the subsonic region.

Axial variation of Mach number.—The axial variation of Mach number predicted when no downstream grid is used appears in figure 14. Index j varies from 2 to 50 in this figure. As for C_p in figure 13, the variation of Mach number in figure 14 is identical to that for M shown in figure 9(a) up to the onset of the shock wave.

Effect of Assuming an Inviscid Wall

Contour plots.—With the assumption of an inviscid wall (slip), the contour plots of M, p, and P_0 of figure 15 were obtained. Little effect is discernible for M and p in figures 15(a) and 15(b) in comparison with figures 6(a) and 6(b), respectively. Effect of the wall assumption does not permeate much beyond the profile for these variables.

Figure 15(c) reveals that the main difference for P_0 is the spreading of its contours near the profile. As in figures 6(c), figure 15(c) clearly indicates the location of the shock wave.

Coefficient of pressure.—A comparison of the effect of the two wall assumptions on the coefficient of pressure on the airfoil outline is presented in figure 16. This figure shows little effect, although this is the location where any effect should be discernible.

Effect of Coarser Grids

Lateral density (varying index j).—The use of coarser grids in the lateral direction (j = 30, j = 60, and j = 120) was mentioned previously. Contour plots for these grids were made, but are not presented here in the interest of brevity. The main effect revealed by the contour plots is that the coarser the grid, the higher is the predicted value of far field static pressure.

Coefficient of pressure.—Figure 17 presents the coefficient of pressure for all four lateral grid densities investigated. As expected, the coarser the grid, the greater the deviation from the densest 113 x 960 grid results. The onset of the shock wave for the 113 x 120 grid coincides with that for the most dense grid. However, the two coarser grids predict the occurrence of the shock wave to be about 0.1 foot farther downstream. Beyond about 0.7 foot, the curves for all four grid densities are similar.

Radial downstream density (varying index i).—The effects of radial density in the downstream grid were investigated by using 20 i-lines instead of the previous 40 i-lines. That is, 73 total radial lines will be compared with using 113 total radial lines. Use of all four lateral grid densities was again made. As above, contour plots were made but are not presented herein. The shock wave was well defined by using all four of the lateral grid densities. The contour plots using 73 radial grid lines were virtually the same as when using 113 lines. Furthermore, the axial variation of the coefficient of pressure when using 73 radial lines was identical to that for 113 lines shown in figure 17.

It was shown above that not using a downstream grid had a large effect on conditions from the beginning of the shock wave and beyond it. However, the radial density of the downstream grid had no effect on predicted results.

Effect of Decreased Grid Height

The grid height yH of 4 feet used in all previous calculations, and shown in figure 2(a), was halved and quartered in this section. The number of lateral grid lines, 960, however, remained the same. Thus, the lateral grid spacing was halved and quartered to 1/40 and 1/80 inch, respectively, for $yH = 2$ and $yH = 1$ foot. Meanwhile, in each instance the radius $R = yH$. Presumably, doubling and quadrupling the number of lateral grid lines within the boundary layer should improve the resolution in this region. However, the far field resolution may be adversely affected by not extending the grid as far away from the airfoil. The following presentations will resolve these issues. Figures 18(a) and 18(b) show the grid near the airfoil for $yH = 2$ and $yH = 1$, respectively.

Contour plots.—Figures 19(a) and 19(b) present contour plots for Mach number and static pressure, respectively, for $yH = 2$. The corresponding plots for $yh = 1$ appear in figures 19(c) and 19(d). The former two figures reveal that in comparison with figures 6(a) and 6(b), setting $yH = 2$ while halving the lateral grid spacing had little effect. However, further decreasing the extent of the far field to $yh = 1$ resulted in failure to define the shock wave, as shown by figures 19(c) and 19(d). This failure occurred despite quadrupling the number of lateral grid lines within the boundary layer.

Coefficient of pressure.—A comparison of the coefficient of pressure for these three grid heights appears in figure 20. When $yH = 4.0$ feet, figure 20 reveals a higher maximum value for $-C_p$. Also, the onset of the shock wave occurs slightly farther downstream, and it terminates at a lower static pressure for $yH = 4$ than for $yH = 2$. Figure 20 thus indicates that using $yH = 4$ predicts a stronger shock than $yH = 2$. The triangle symbols in figure 20 further reveal the inability of using $yH = 1$ to capture the shock wave. This failure is actually gratifying, because it highlights the importance of using a grid that extends far enough into the far field.

Comparisons With the Literature

Validation of the results for the 113 x 960 grid is presented by making certain comparisons with numerical and experimental results from the literature.

Contour plot comparison.—Figure 21 taken from reference 7 is a Mach number contour plot to be compared with figure 6(a). The results presented in figure 21 were derived by applying a multi-sweep relaxation procedure to the Reduced Navier-Stokes equations (RNS). The conditions prescribed for the work investigated for the current report were purposely set to match those used in producing figure 21. Furthermore, the current investigation made calculations twice as far downstream and four times as far in the far field as those shown in figure 21.

Nevertheless, figure 6(a) closely matches figure 21, including rendition of the shock wave. In fact, RNS results should more logically be compared with those of the more sophisticated WIND code as a standard.

Coefficient of pressure comparison.—The coefficient of pressure for the 113 x 960 grid presented in figure 7 is shown again in figure 22 by the circle symbols. This figure presents a comparison of the current WIND results with the numerical results of references 7 and 8, that used the RNS equations, and with the experimental results of reference 9. The current WIND results predict higher values of $-C_p$ upstream of the shock wave than the others. Figure 22 reveals that all four methods shock down to about the same value of $-C_p$. However, the experimental results of reference 9, which are the standard for comparison, and shown by the diamond symbols, yielded the steepest slope for the shock wave. Notice that reference 9 has one more data point between $x/c = 0.4$ and 0.5 than the WIND results. Discrepancies with the experimental data remain unresolved. All four investigations essentially coincide downstream of the shock wave. Thus, figure 22 reveals that all three numerical methods yielded reasonable agreement with the experimental results of reference 9.

Comparison of velocity squared vs x.—Figure 23 presents the axial variation of the square of the velocity magnitude on the profile. The WIND results are compared here with the curve previously displayed in figure 1. The WIND results are from the inviscid wall run, which calculated velocity at $j = 1$. The latter results have yielded a curve shaped similar to that for $-C_p$. Reference 5 does not specify the details of its calculated curve for V**2. Reference 5 states that its results were derived from the potential flow method of Theodorsen reported in references 10 and 11. Nevertheless, the prescribed curve does not provide for the reality of the shock wave, that is prominently displayed by WIND.

Summary of Observances

1.) No separation was observed on the airfoil, nor was a downstream vortex.

2.) Within the boundary layer, the stagnation pressure dropped deeply and steeply on the airfoil itself from the nose to the shock wave. This effect was much less drastic off the profile, but still within the boundary layer.

3.) When no downstream grid was used, the predicted shock wave appeared 0.2 feet farther along the profile and was steeper than when a downstream grid was used.

4.) There was very little difference between using a viscous wall assumption and an inviscid wall.

5.) The use of coarser lateral grids predicted higher static pressure in the far flow field. Although the use of coarser lateral grids adequately defined the shock wave, they predicted the onset to be about 0.1 foot farther downstream than dense grids.

6.) No effect was observed between using a coarse and a dense downstream radial grid.

7.) Predicted far field conditions were not affected when the grid height was changed from 4 feet to 2 feet. The effects within the boundary layer were minor. However, using $yH = 1$ resulted in a failure to define the shock wave, despite quadrupling the number of lateral grid lines in the boundary layer.

8.) Mach number contours provided by the current WIND investigation closely matched those predicted in the literature. Likewise, there was good agreement of the current results for C_p with those taken from two numerical references and one experimental reference. However, there was a wide disparity in the axial variation of the square of the velocity magnitude computed by WIND with the original potential flow design.

References

1. Bush, R.H., Power, G.D., and Towne, C.E.: "WIND: The Production Flow Solver of the NPARC Alliance," AIAA Paper 98–0935, 1998. Also WIND Home Page: http://www.grc.nasa.gov/www/winddocs/user/files.html.
2. Walatka, Pamela P., Buning, Pierer G., Pierce, Larry, and Elson, Patricia A.: "PLOT3D USER'S MANUAL," NASA, March 1990.
3. Towne, Charles E.: "PLOTC USER'S MANUAL: VERSION 2.3," NASA Internal Memorandum, April, 1994.
4. Jacobs, Eastman N., Ward, Kenneth E., and Pinkerton, Robert M.: "The Characteristics of 78 Related Airfoil Sections from Tests in the Variable-density Wind Tunnel," NACA Rept. No. 460, 1932.
5. Abbott, Ira H., and Von Doenhoff, Albert E.: "Theory of Wing Sections," Dover Publications, Inc., New York, 1959.
6. Ames Research Staff: "Equations, Tables, and Charts For Compressible Flow," NACA Rept. No. 1135, 1953.
7. Reddy, D.R. and Rubin, S.G. "Subsonic/Transonic Viscous/Inviscid Relaxation Procedures for Strong Pressure Interactions," AIAA–84–1627, June, 1984.
8. Rubin, S.G., Celestina M., and Khosla, P.K. "Second Order Composite Velocity Solution for Large Reynolds Number Flows," AIAA Paper No. 84-0172, January 1984.
9. Thibert, J.J., Grandjacques, M., and Ohman, L.H. "Experimental Data Base For Computer Program Assessment," AGARD Advisory Report No. 138, NATO.
10. Theodorsen, Theodore: "Theory of Wing Sections of Arbitrary Shape," NACA Rept. No. 411, 1931.
11. Theodorsen, Theodore, and Garrick, I.E. "General Potential Theory of Arbitrary Wing Sections," NACA Rept. No. 452, 1933.

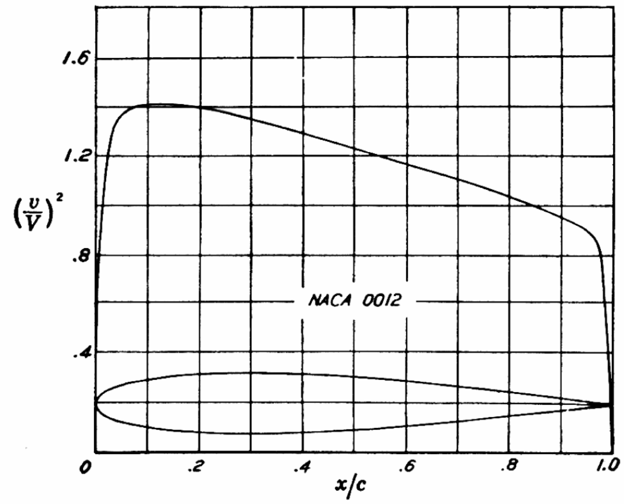

x (per cent c)	y (per cent c)	$(v/V)^2$	v/V	$\Delta v_a/V$
0	0	0	0	1.988
0.5	.....	0.640	0.800	1.475
1.25	1.894	1.010	1.005	1.199
2.5	2.615	1.241	1.114	0.934
5.0	3.555	1.378	1.174	0.685
7.5	4.200	1.402	1.184	0.558
10	4.683	1.411	1.188	0.479
15	5.345	1.411	1.188	0.381
20	5.737	1.399	1.183	0.319
25	5.941	1.378	1.174	0.273
30	6.002	1.350	1.162	0.239
40	5.803	1.288	1.135	0.187
50	5.294	1.228	1.108	0.149
60	4.563	1.166	1.080	0.118
70	3.664	1.109	1.053	0.092
80	2.623	1.044	1.022	0.068
90	1.448	0.956	0.978	0.044
95	0.807	0.906	0.952	0.029
100	0.126	0	0	0
L.E. radius: 1.58 per cent c				

NACA 0012 Basic Thickness Form

Figure 1.—NACA 0012 airfoil from Ref. 5.

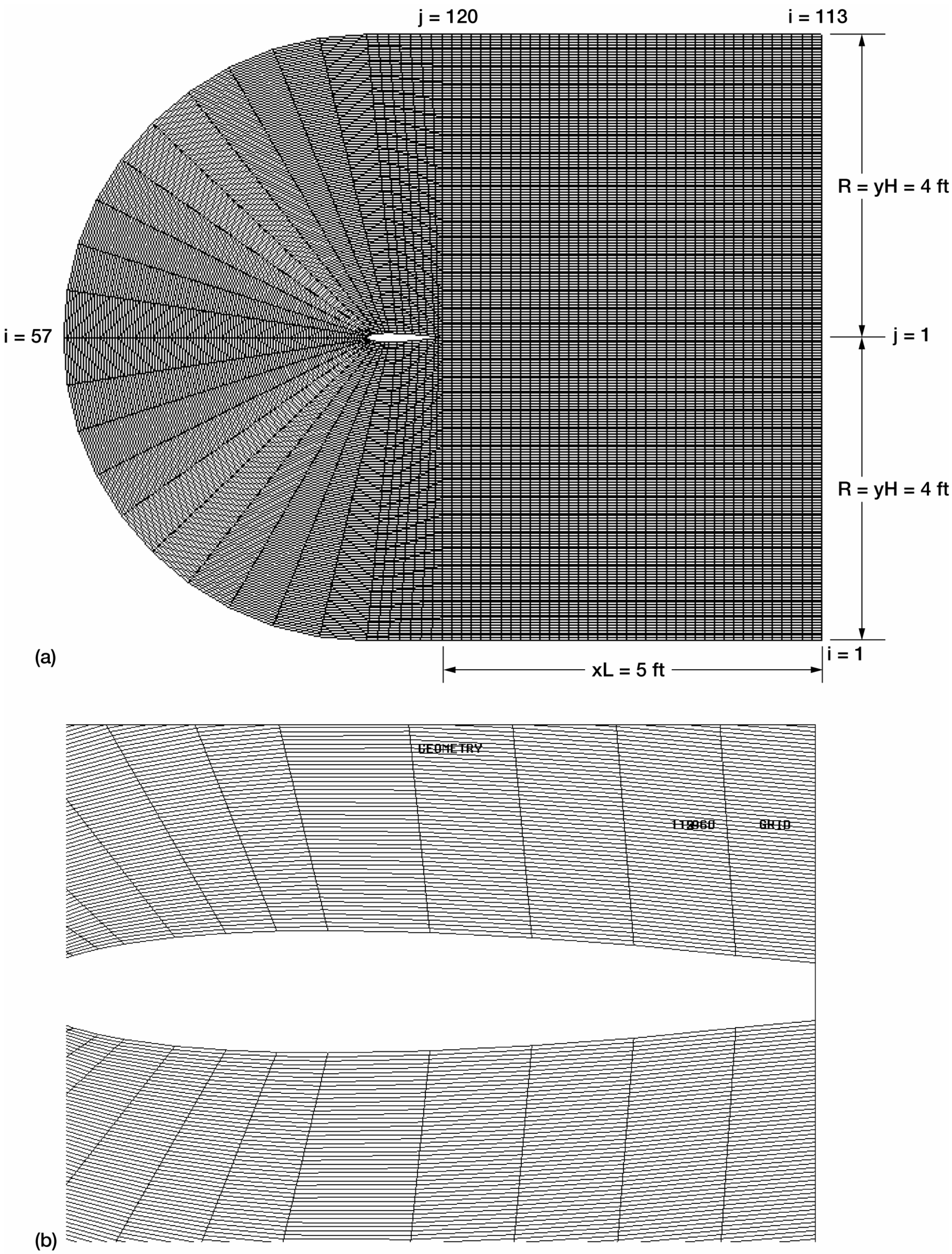

Figure 2.—Grids around NACA 0012 airfoil. (a) 113×120 grid. (b) 113×960 grid.

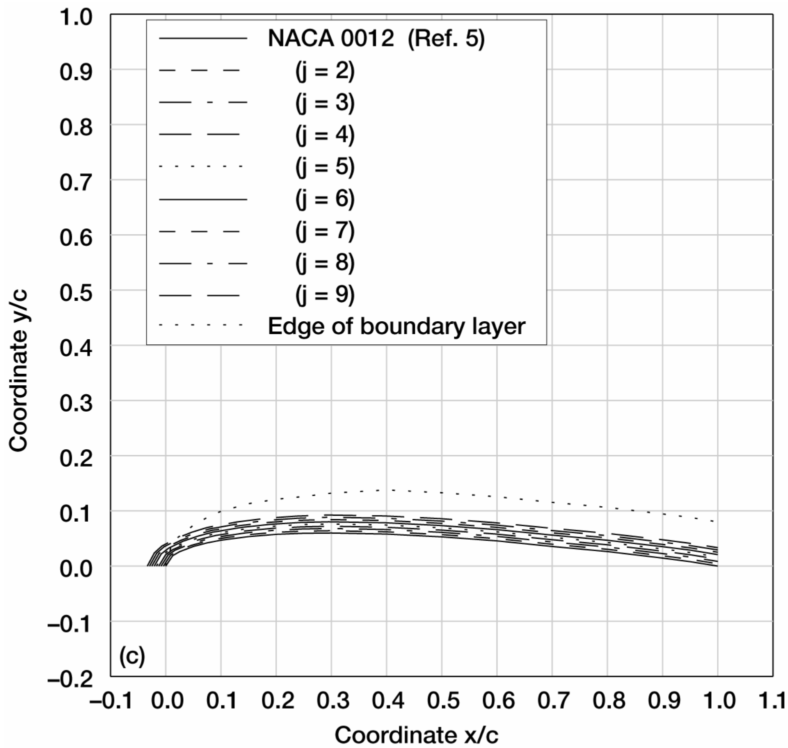

Figure 2.—Grids around NACA 0012 airfoil, concluded. (c) NACA 0012, 8 j-lines, and edge of boundary layer.

```
! GMANPRE - Version 6.144 (last changed 2001/06/05 19:19:52)
 1
 FILE nat.cgd
 ZONE 1
 UNITS FSS
   BOUNDARY I1
     OUTFLOW
     UPDATE
   BOUNDARY IMAX
     OUTFLOW
     UPDATE
   BOUNDARY J1
     SUBAREA I1 I39
       COUPLED TO ZONE 1 BOUNDARY J1
       UPDATE
     SUBAREA I40 I74
       VISCOUS WALL
       UPDATE
     SUBAREA I75 I113
       COUPLED TO ZONE 1 BOUNDARY J1
       UPDATE
   BOUNDARY JMAX
     FREESTREAM
     UPDATE
CHECK BOUNDARY
```

Figure 3.—Grid management (GMAN) file.

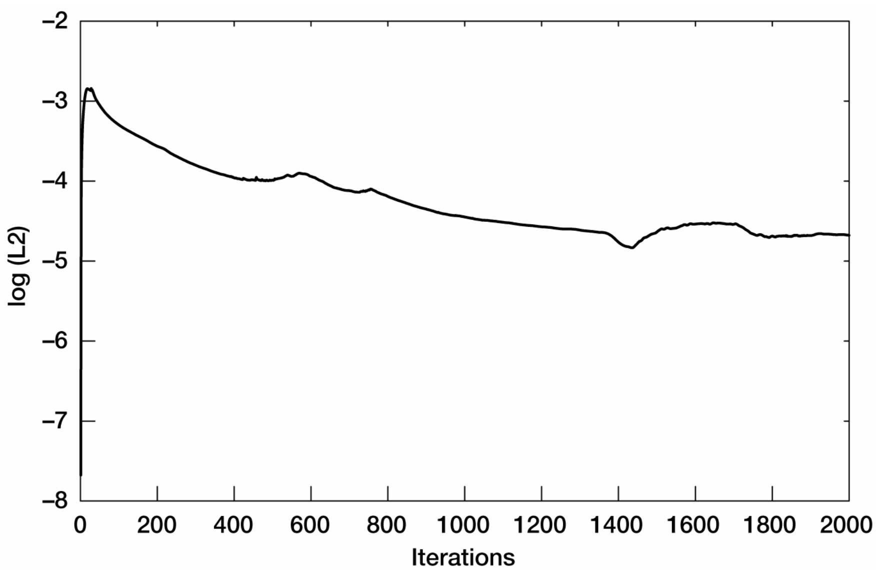

Figure 4.—Convergence history of residuals.

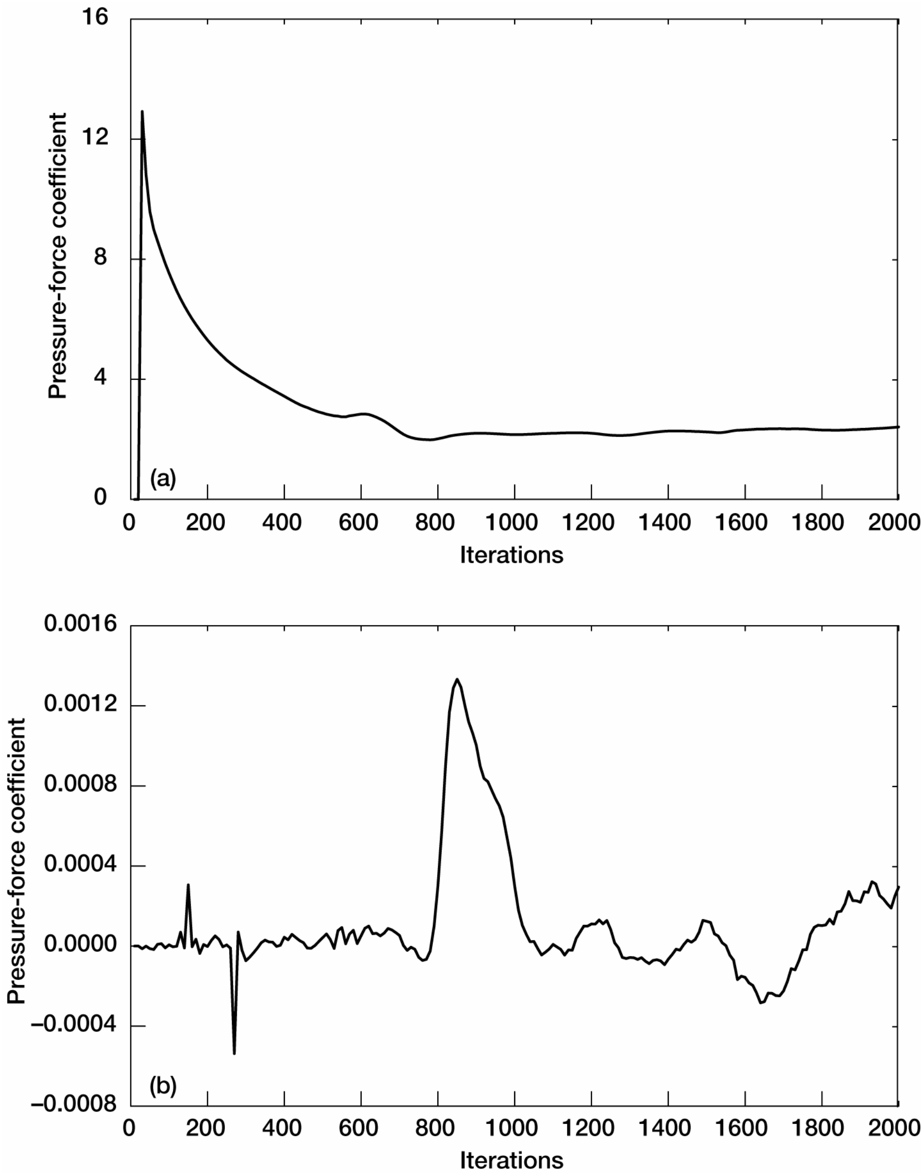

Figure 5.—Convergence history of pressure force coefficients. (a) Drag. (b) Lift.

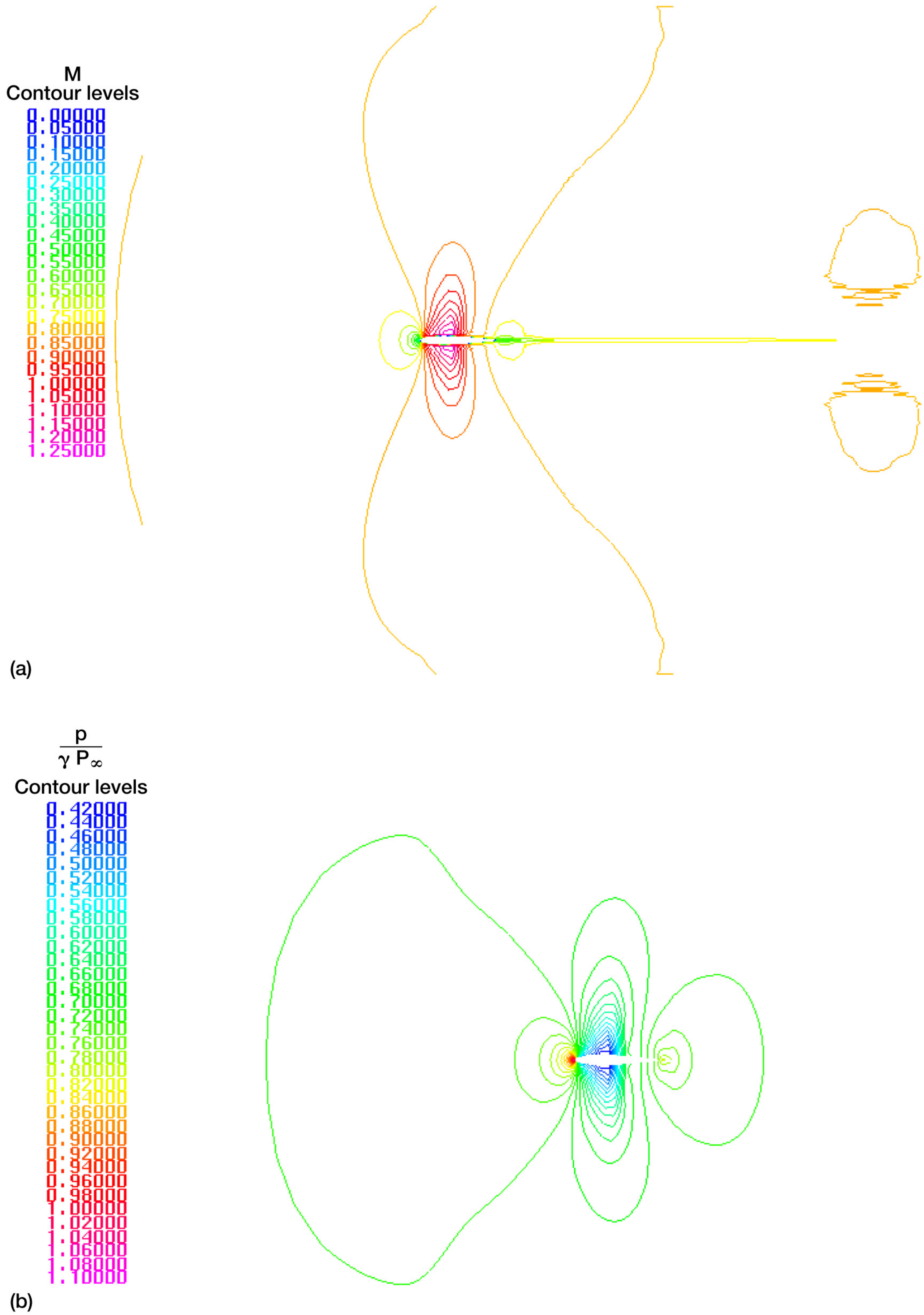

Figure 6.—Contour plots for 113×960 grid. (a) Mach number. (b) Static pressure.

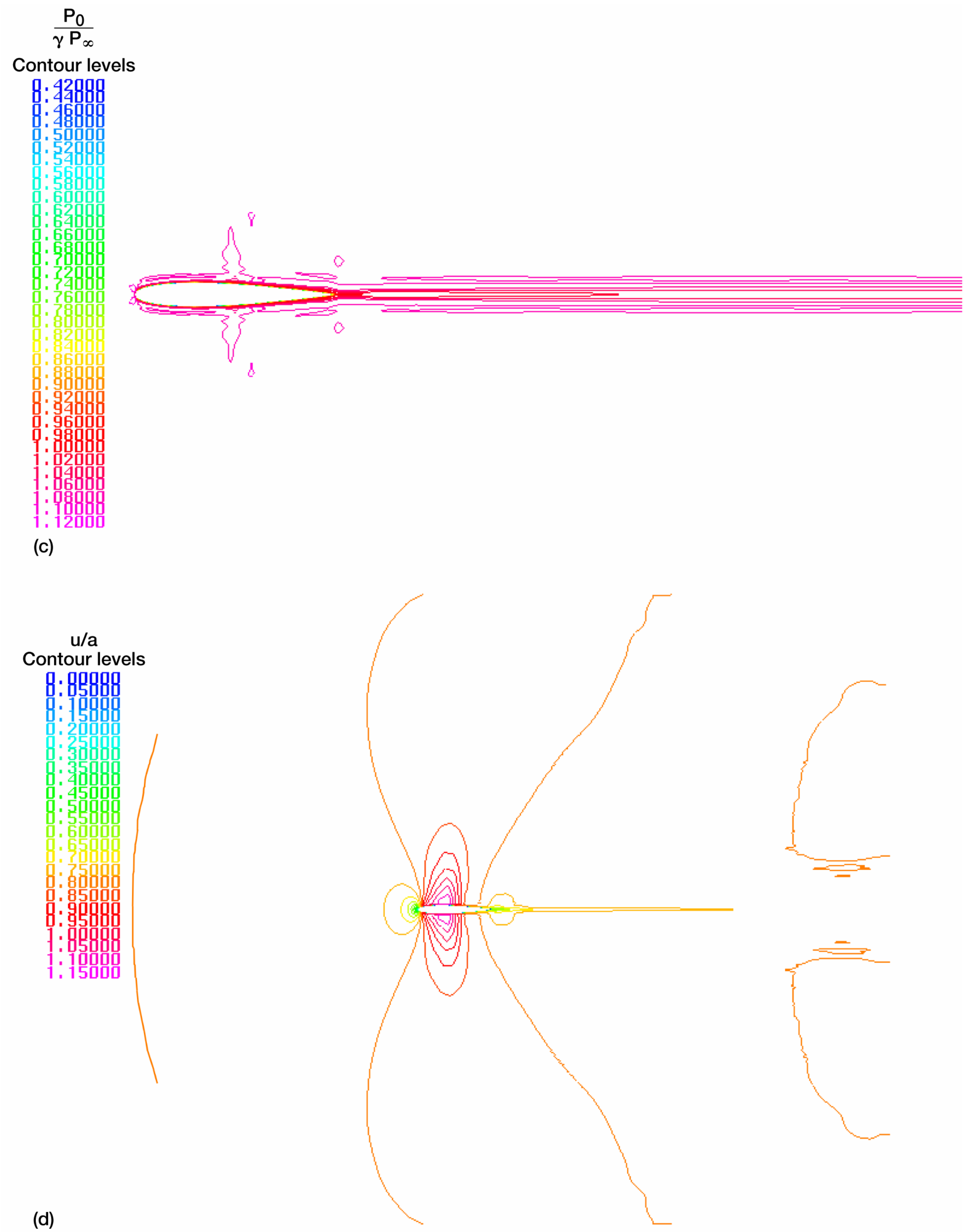

Figure 6.—Contour plots for 113×960 grid, concluded. (c) Stagnation pressure. (d) Axial component of velocity.

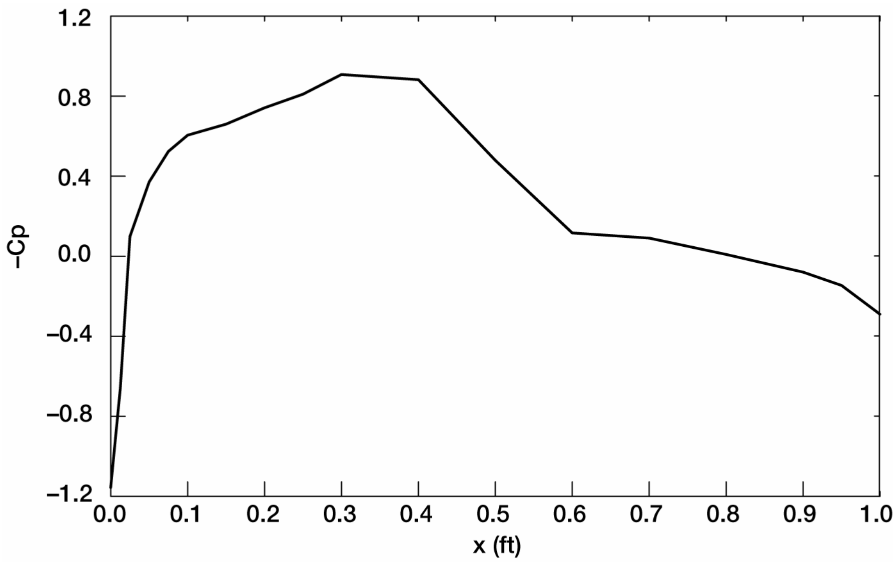

Figure 7.—Coefficeint of pressure for 113×960 grid.

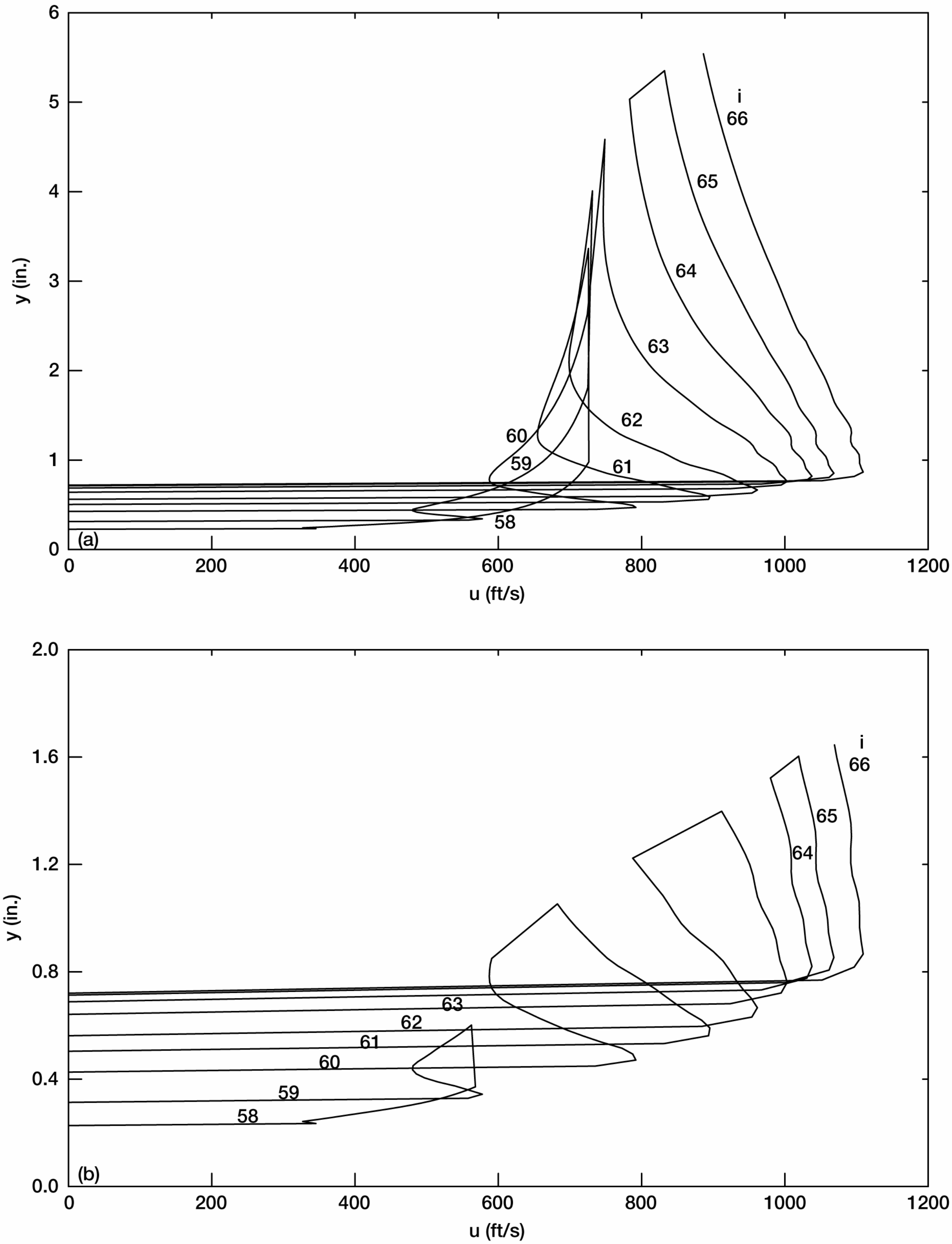

Figure 8.—Variation of axial velocity with y. (a) Fore part of airfoil; j_{max} = 100. (b) Fore part of airfoil; j_{max} = 20.

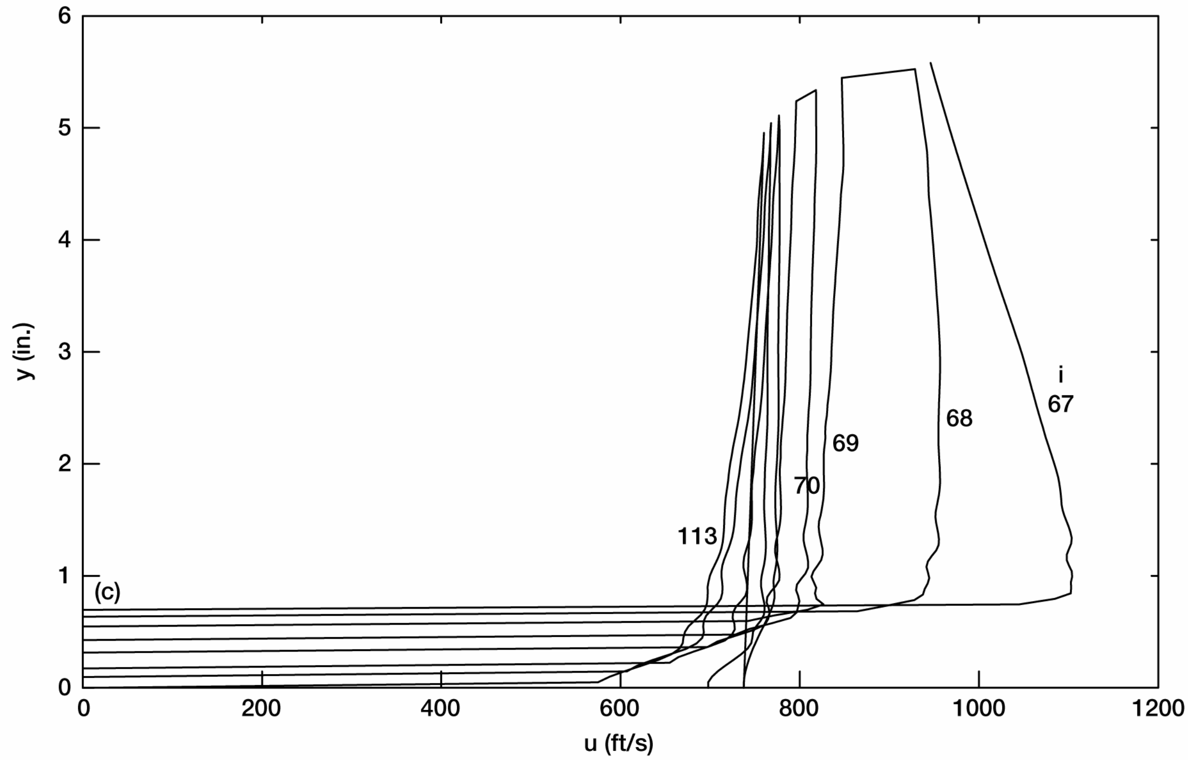

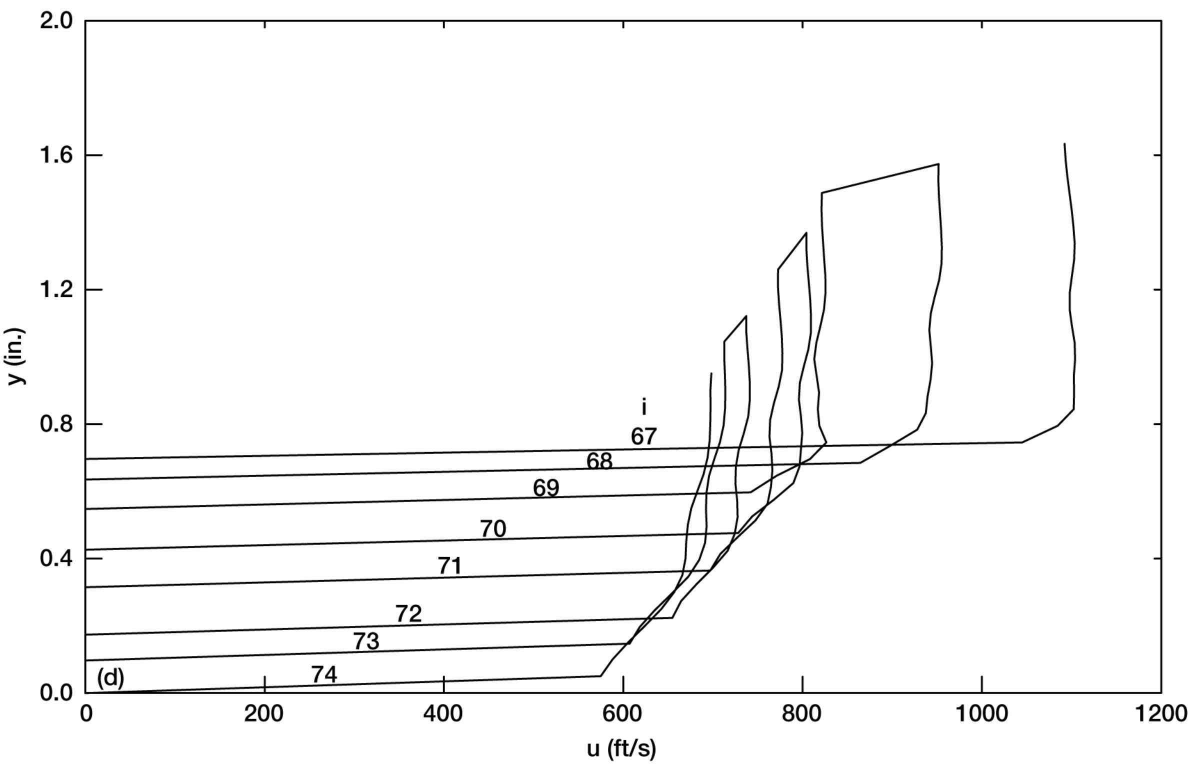

Figure 8.—Variation of axial velocity with y, concluded. (c) Rear of airfoil; j_{max} = 100. (d) Rear of airfoil; j_{max} = 20.

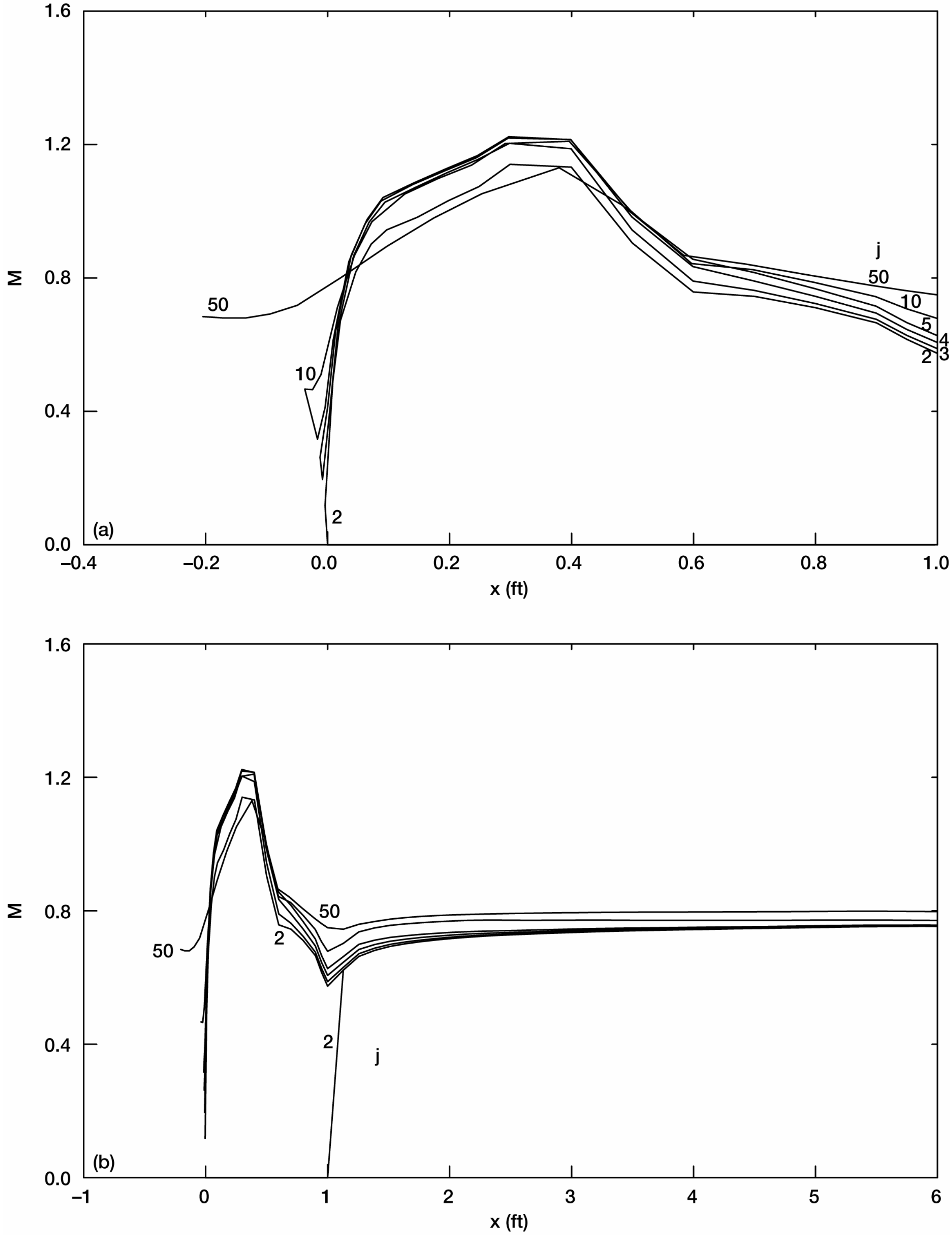

Figure 9.—Axial variation of Mach number; j = 2 to 50. (a) Over airfoil. (b) Over entire grid range.

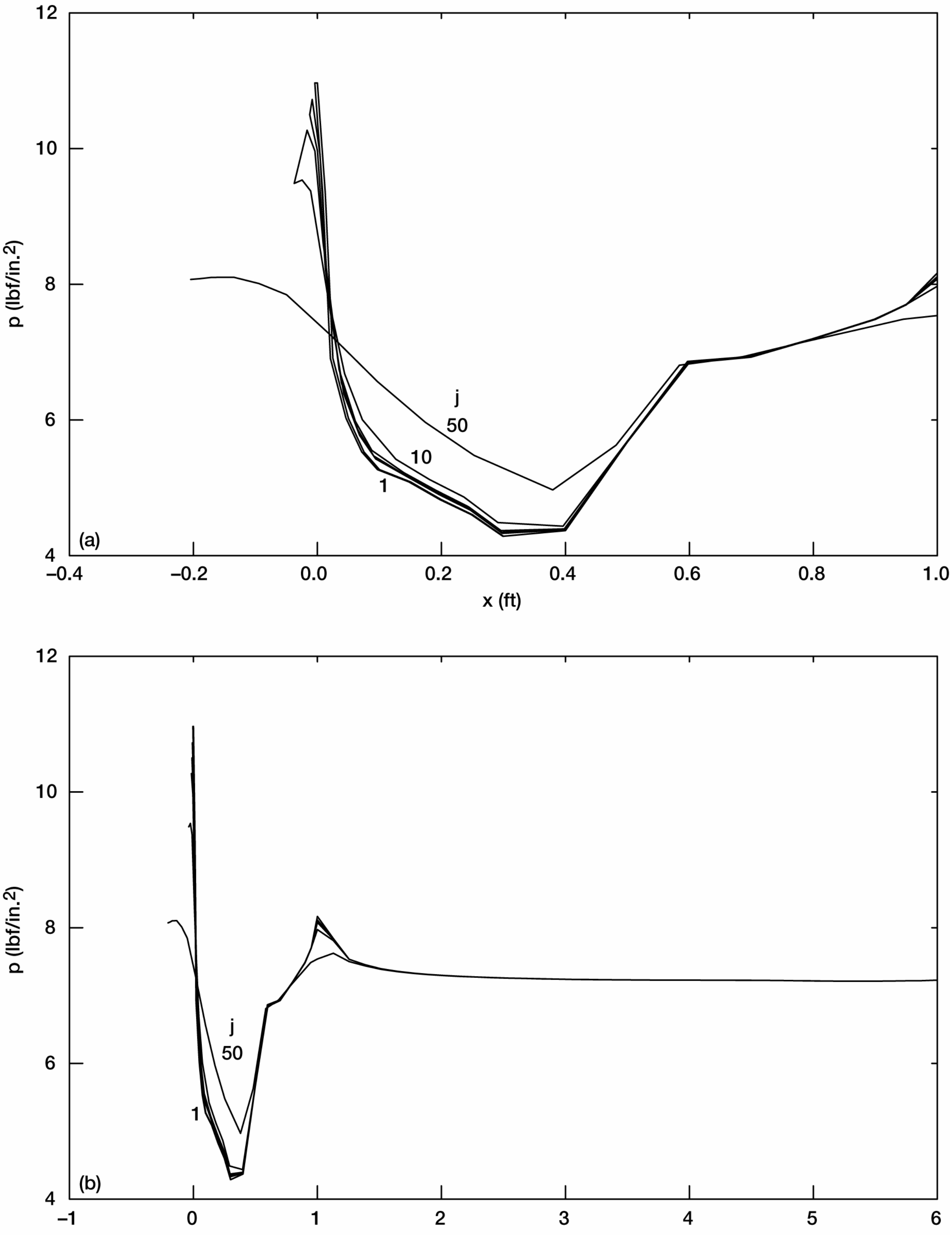

Figure 10.—Axial variation of static pressure; j = 1 to 50. (a) Over airfoil. (b) Over entire grid range.

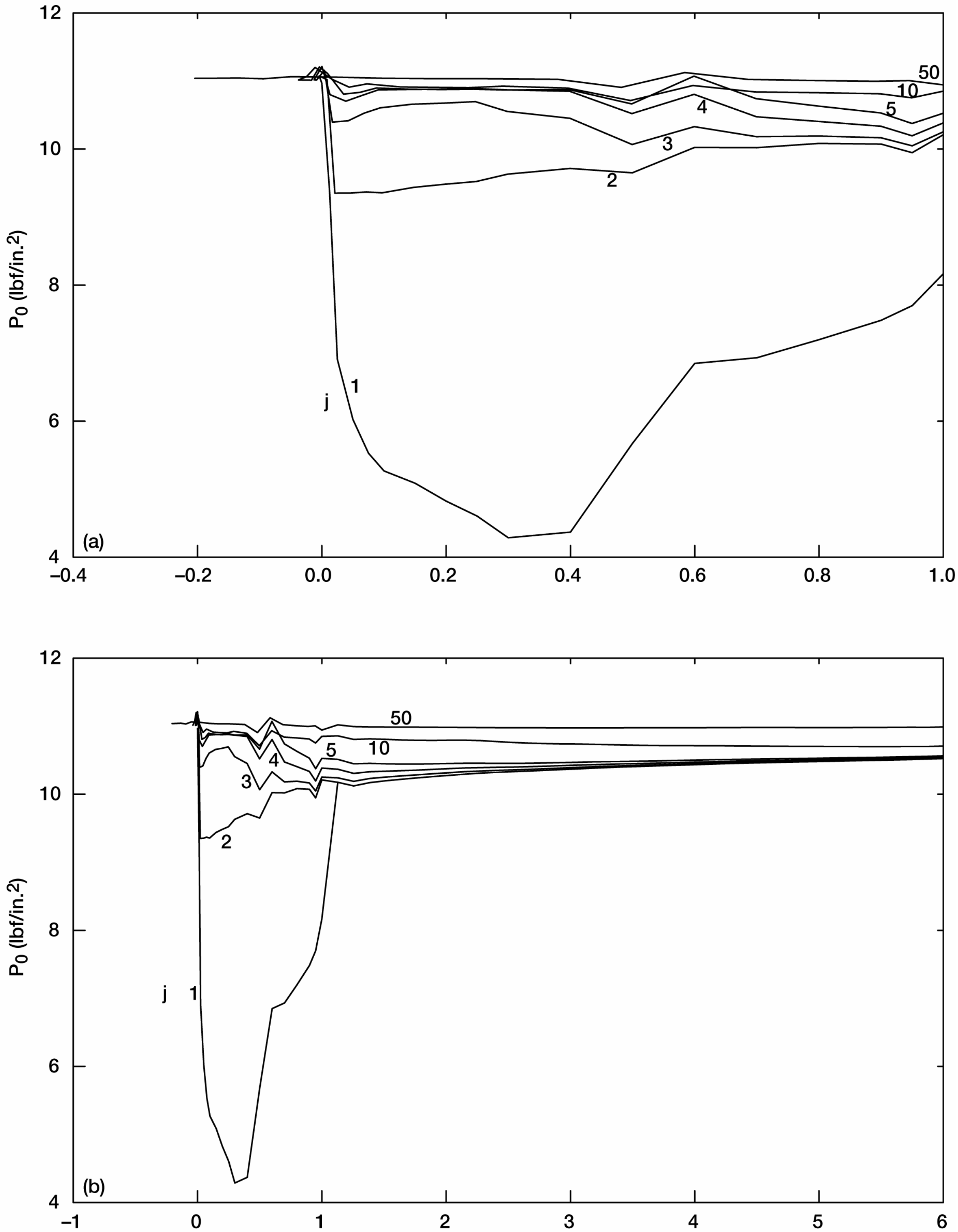

Figure 11.—Axial variation of stagnation pressure; j = 1 to 50. (a) Over airfoil. (b) Over entire grid range.

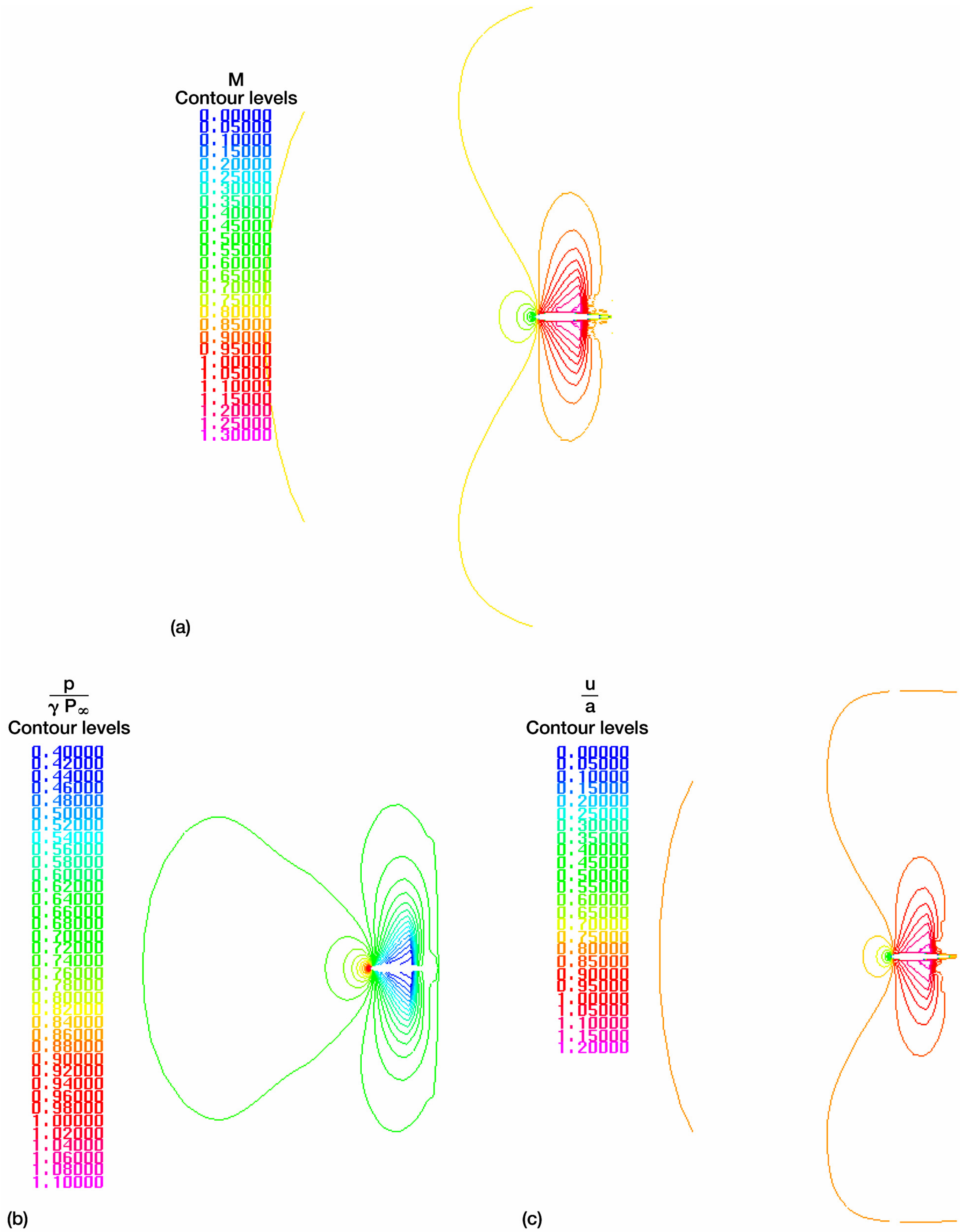

Figure 12.—Contour plots for 35×960 grid (no downstream grid). (a) Mach number. (b) Static pressure. (c) Axial component of velocity.

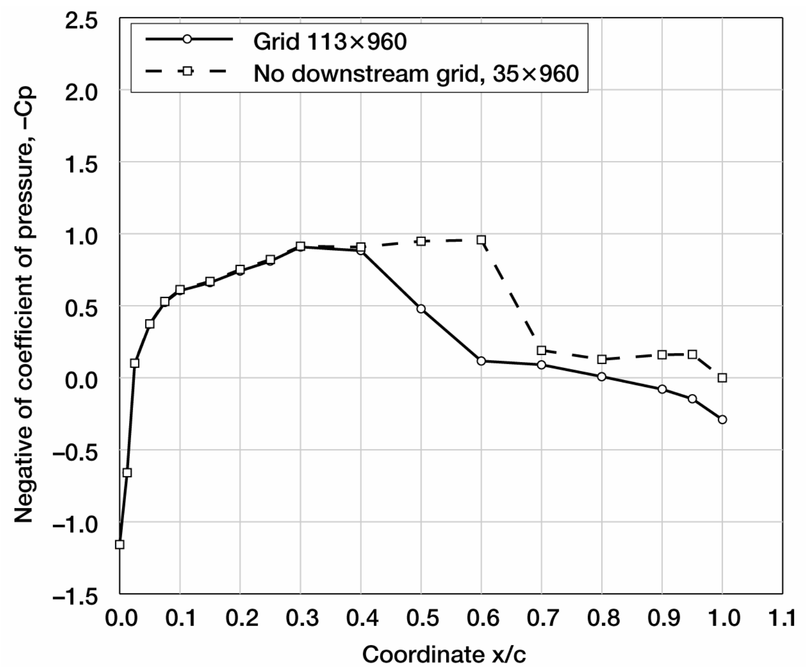

Figure 13.—Comparison of coefficient of pressue for no downstream grid.

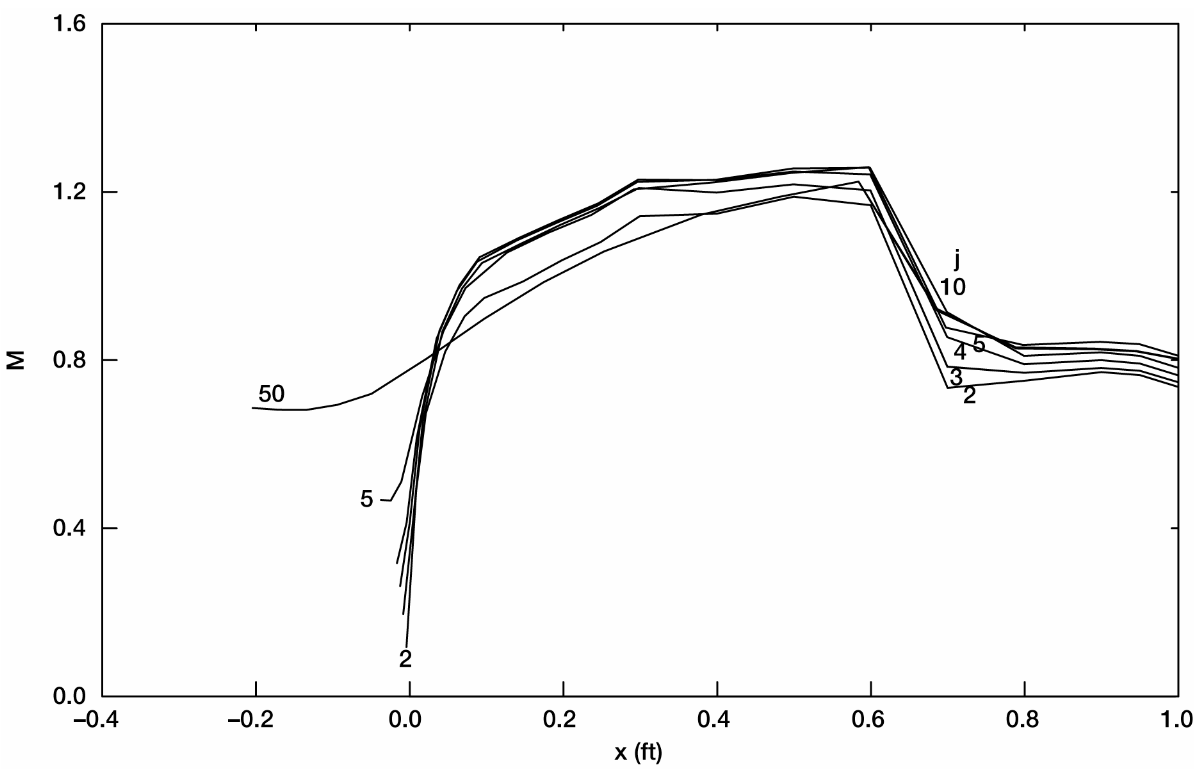

Figure 14.—Axial variation of Mach number for no downstream grid, 35×960.

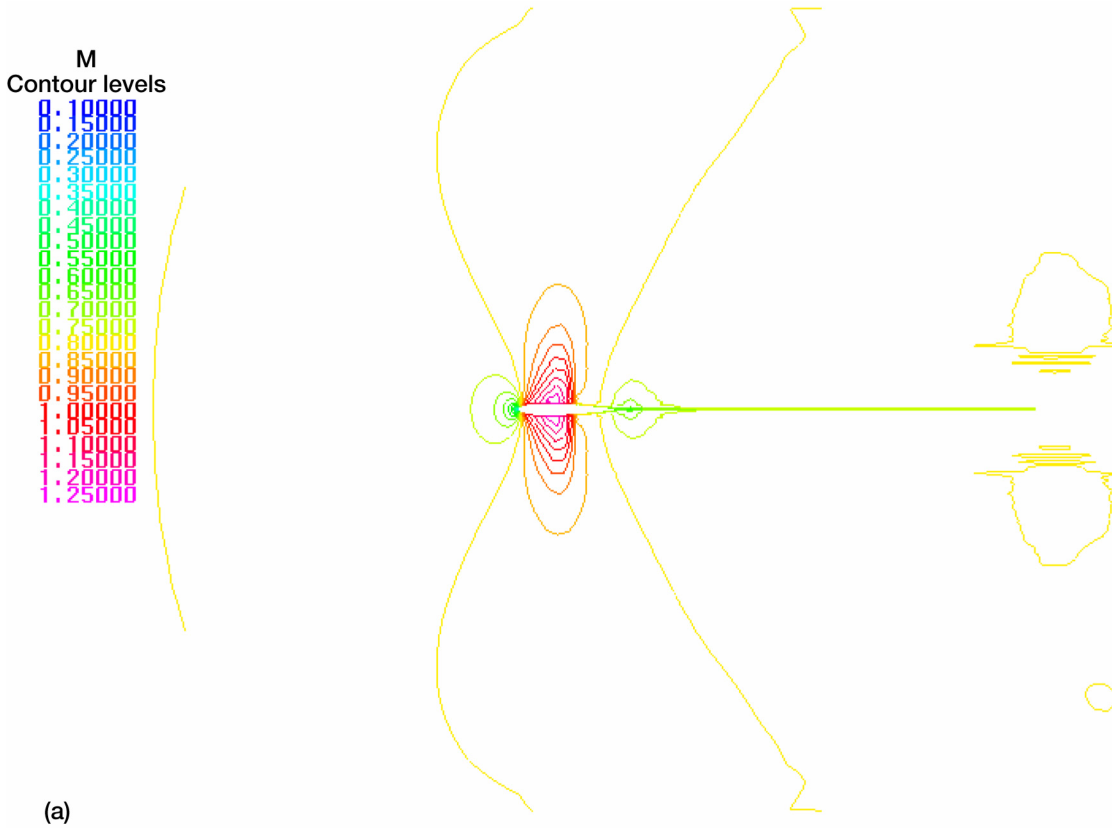

(a)

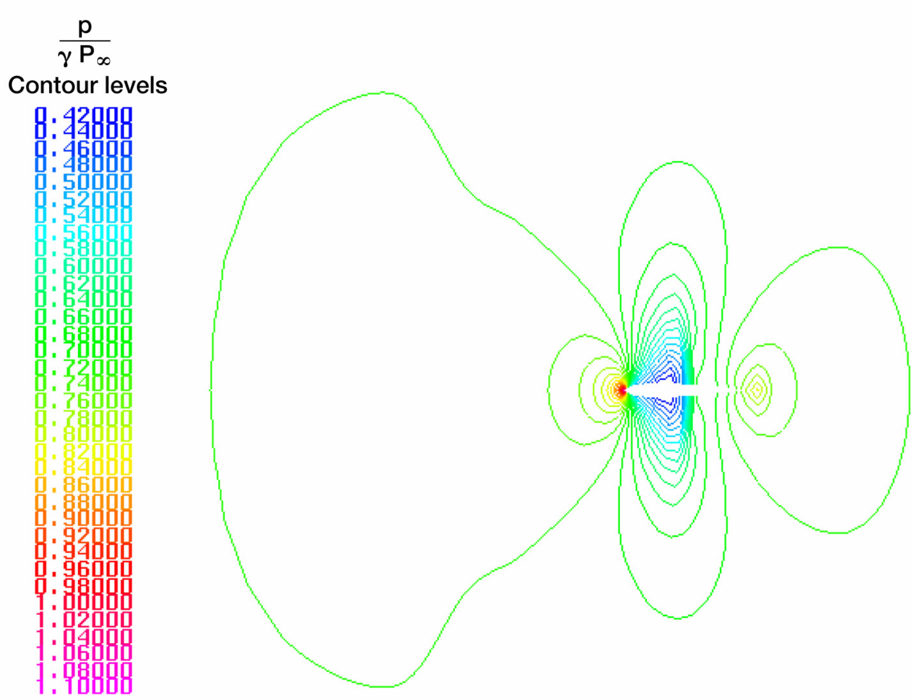

(b)

Figure 15.—Contour plots for 113×960 grid (inviscid wall). (a) Mach number. (b) Static pressure.

Figure 15.—Contour plots for 113×960 grid (inviscid wall), concluded. (c) Stagnation pressure.

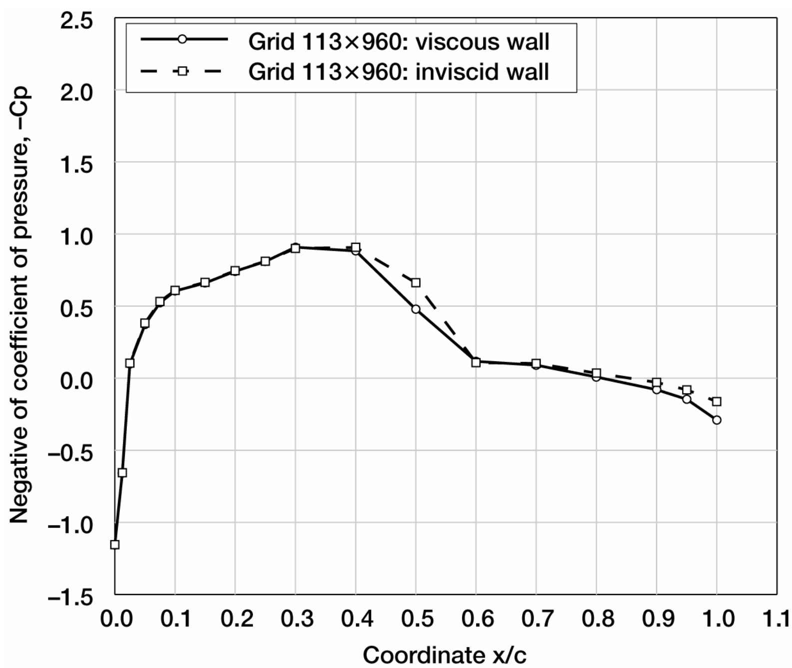

Figure 16.—Comparison of coefficient of pressure for inviscid wall assumption.

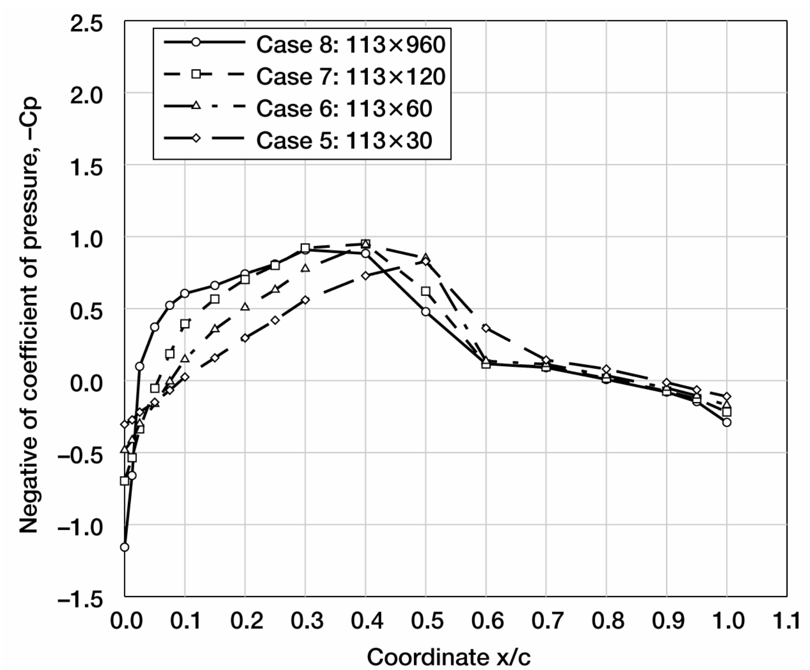

Figure 17.—Comparison of coefficient of pressure for lateral line densities.

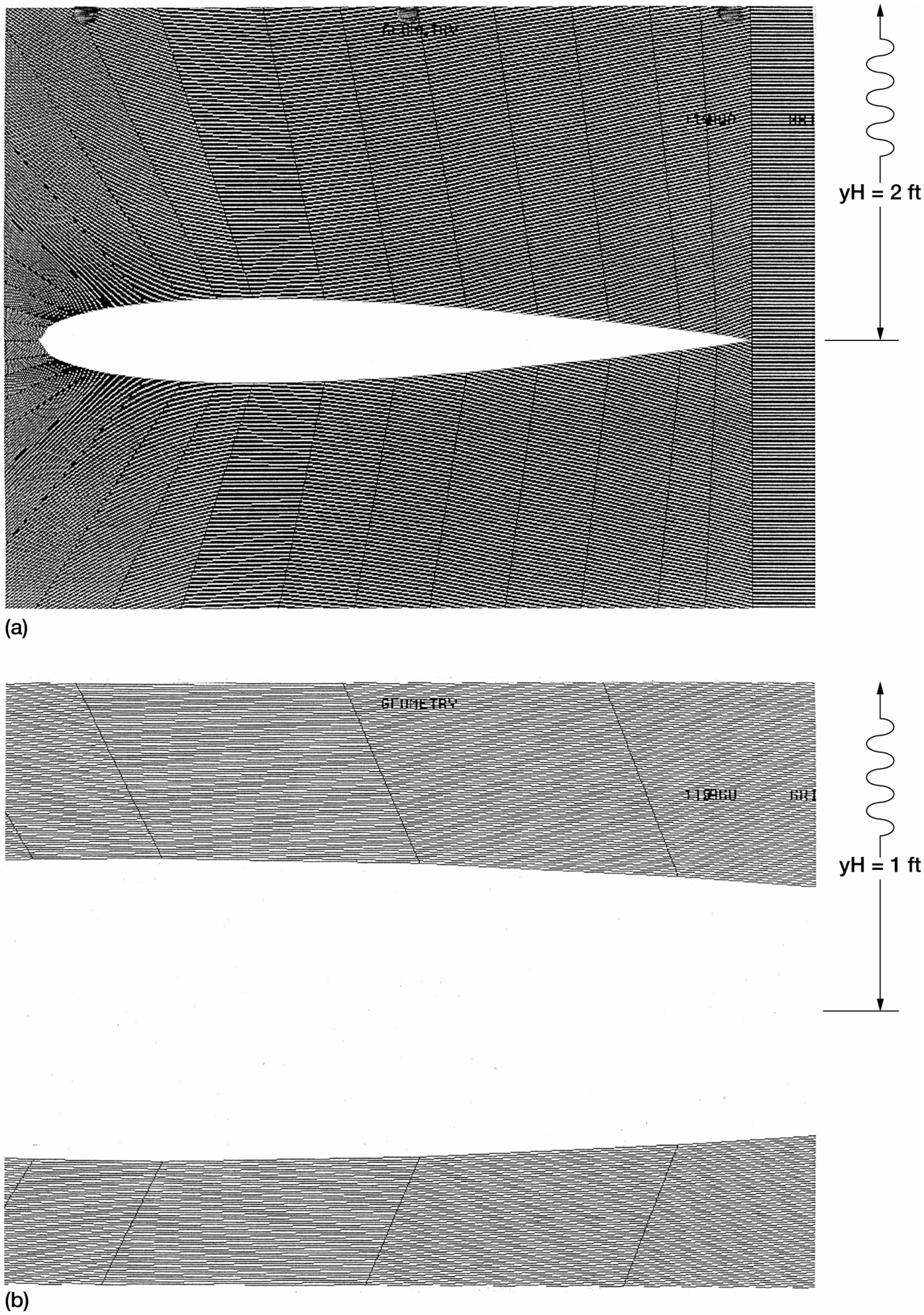

Figure 18.—113×960 grid for 2 values of yH. (a) yH = 2. (b) yH = 1.

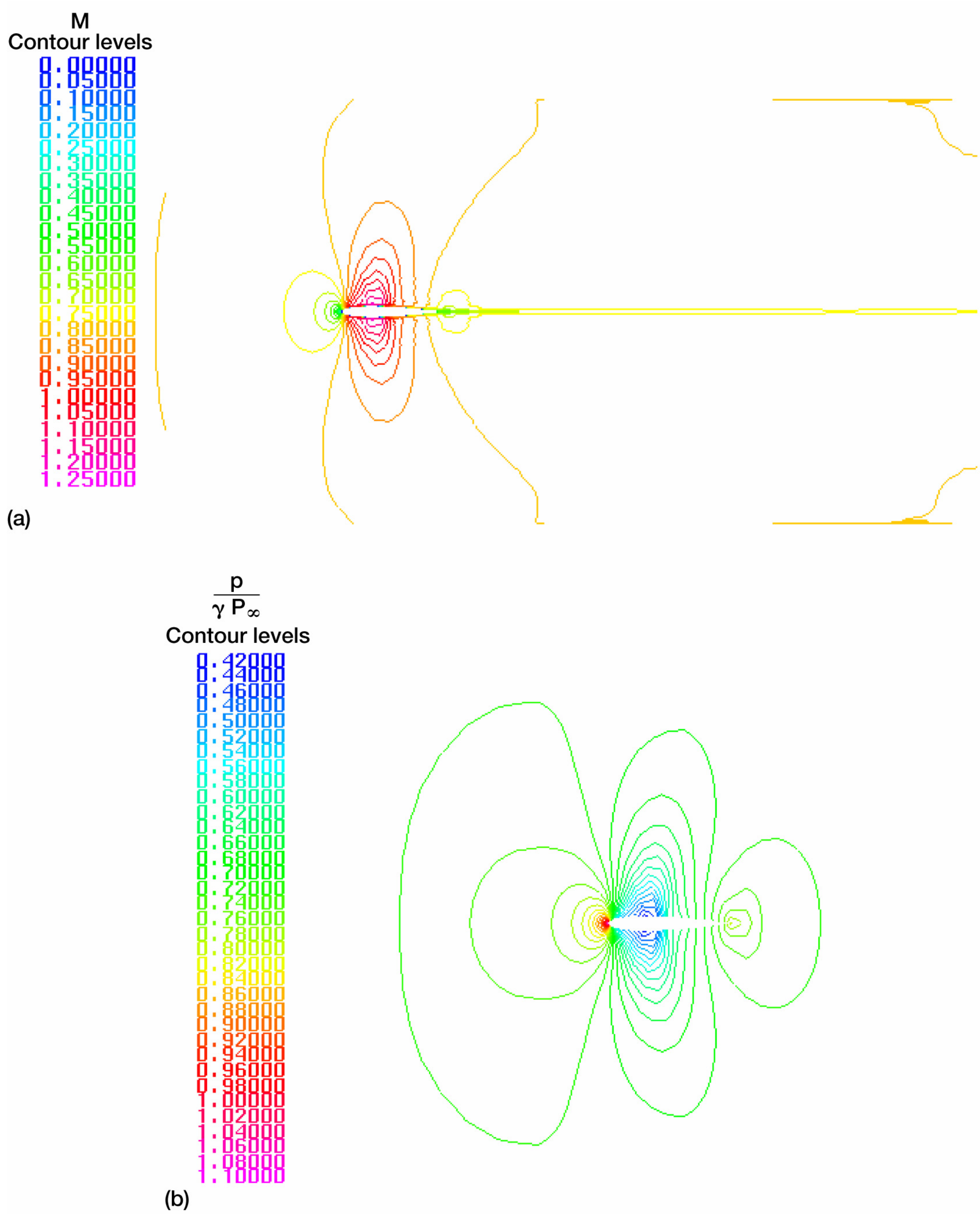

Figure 19.—Contour plots for 113×960 grid for 2 values of yH. (a) Mach number; yH = 2. (b) Static pressure; yH = 2.

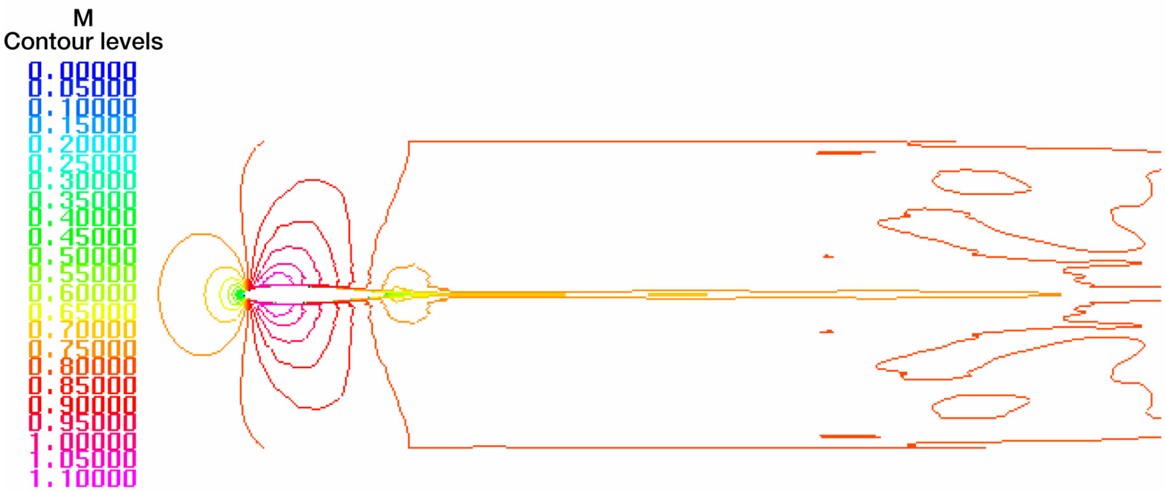

(c)

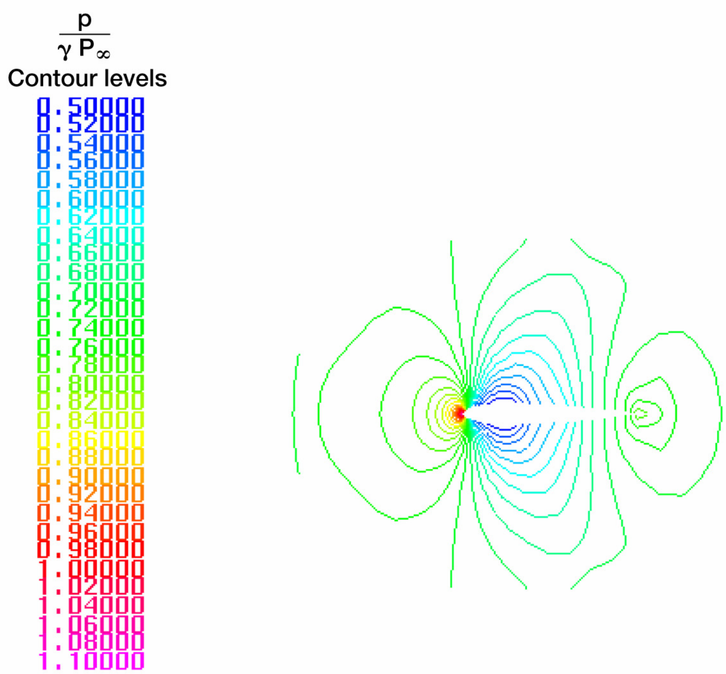

(d)

Figure 19.—Contour plots for 113×960 grid for 2 values of yH, concluded. (c) Mach number; yH = 1. (d) Static pressure; yH = 1.

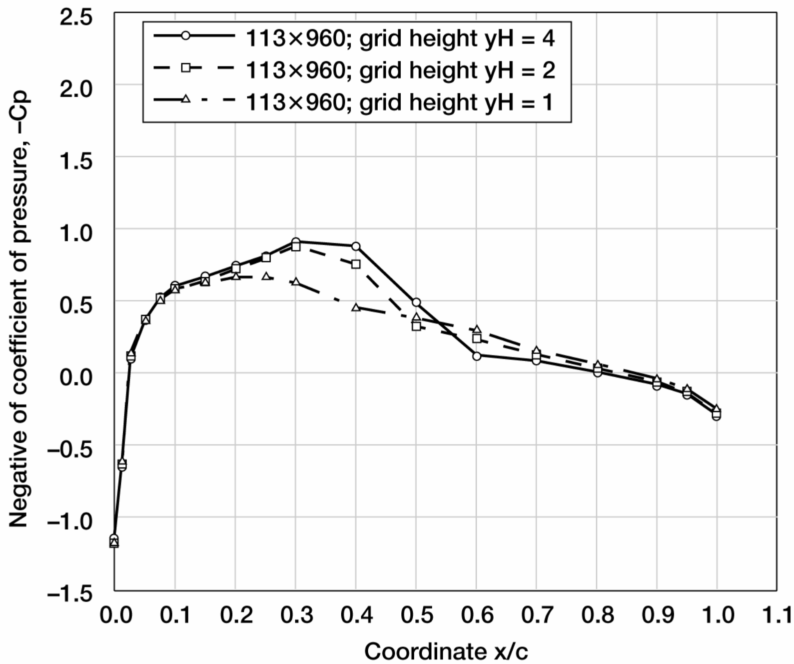

Figure 20.—Comparison of coefficient of pressure for three grid heights.

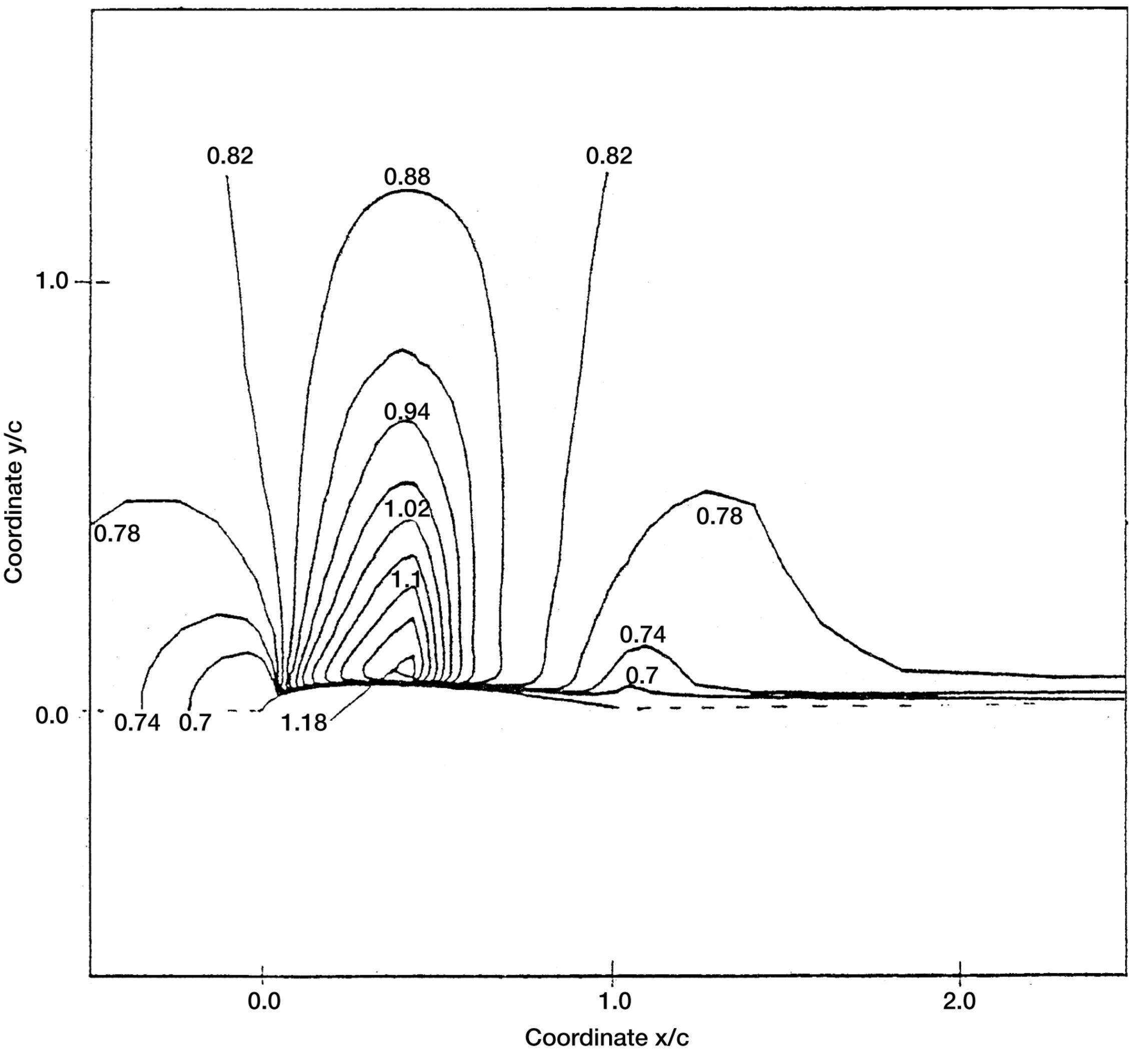

Figure 21.—Contour plot of Mach number calculated by RNS method, taken from Ref. 7.

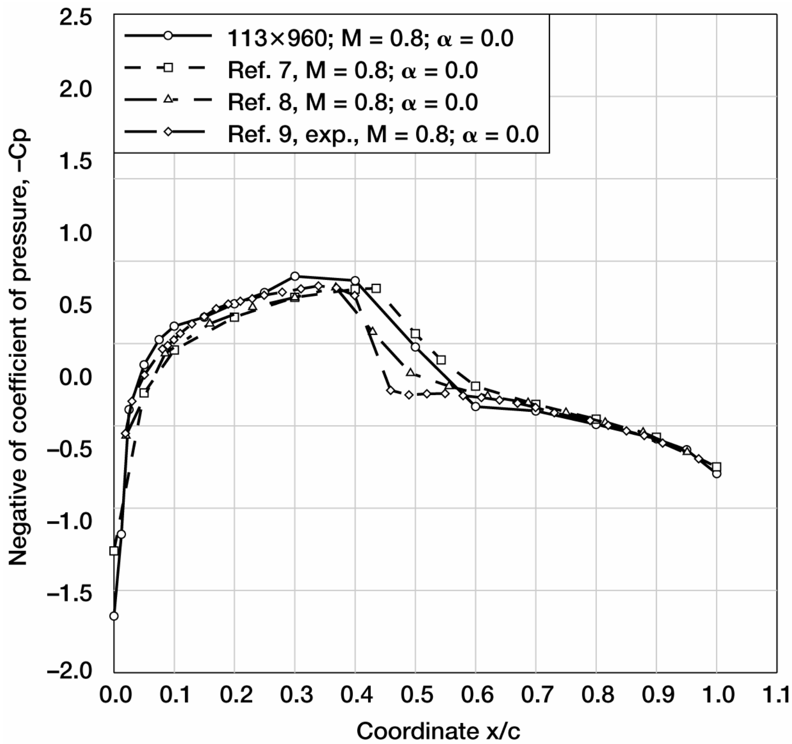

Figure 22.—Comparison of coefficient of pressure with results from the literature.

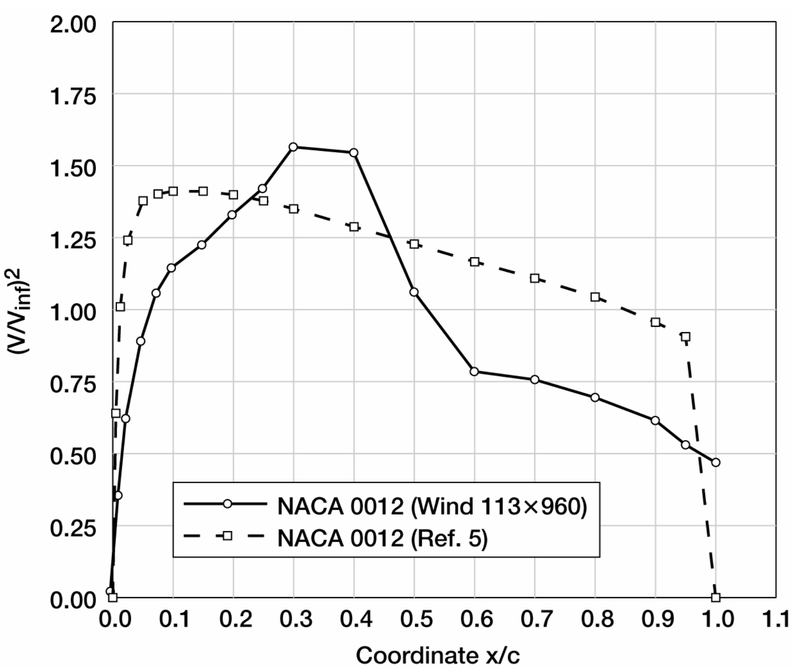

Figure 23.—Comparison of axial variation of square of profile velocity with that prescribed by Ref. 5.

REPORT DOCUMENTATION PAGE

Form Approved
OMB No. 0704-0188

1. AGENCY USE ONLY (*Leave blank*)

2. REPORT DATE
September 2004

3. REPORT TYPE AND DATES COVERED
Technical Memorandum

4. TITLE AND SUBTITLE
Probing Within the Boundary Layer of an Airfoil by Using the Wind Numerical Code

5. FUNDING NUMBERS
WBS–22–708–90–21

6. AUTHOR(S)
Richard H. Cavicchi

7. PERFORMING ORGANIZATION NAME(S) AND ADDRESS(ES)
National Aeronautics and Space Administration
John H. Glenn Research Center at Lewis Field
Cleveland, Ohio 44135–3191

8. PERFORMING ORGANIZATION REPORT NUMBER
E–14728

9. SPONSORING/MONITORING AGENCY NAME(S) AND ADDRESS(ES)
National Aeronautics and Space Administration
Washington, DC 20546–0001

10. SPONSORING/MONITORING AGENCY REPORT NUMBER
NASA TM—2004-213221

11. SUPPLEMENTARY NOTES
Responsible person, Richard H. Cavicchi, organization code 5850, 216–433–5873.

12a. DISTRIBUTION/AVAILABILITY STATEMENT
Unclassified - Unlimited
Subject Category: 02 Distribution: Nonstandard
Available electronically at http://gltrs.grc.nasa.gov
This publication is available from the NASA Center for AeroSpace Information, 301–621–0390.

12b. DISTRIBUTION CODE

13. ABSTRACT ***(Maximum 200 words)***

A detailed boundary layer investigation of an NACA 0012 airfoil was made by applying the WIND code at the NASA Glenn Research Center. Structured C-grids of selected configurations were fitted around the airfoil. Grids with dense spacing to capture the boundary layer provided for obtaining accurate results in this region. Concurrent with the boundary layer investigation, contour plots of overall performance of the airfoil were also obtained. A Mach number of 0.80, a Reynolds number of 4,000,000, and a zero angle of attack were set to correspond with numerical and experimental investigations reported in the literature, for comparison with the overall performance. The results were favorable for both the boundary layer investigations and the performance. As WIND evolves, it is intended to run WIND using unstructured grids to compare such results with the current structured grid results.

14. SUBJECT TERMS
Computational fluid dynamics

15. NUMBER OF PAGES
39

16. PRICE CODE

17. SECURITY CLASSIFICATION OF REPORT	18. SECURITY CLASSIFICATION OF THIS PAGE	19. SECURITY CLASSIFICATION OF ABSTRACT	20. LIMITATION OF ABSTRACT
Unclassified	Unclassified	Unclassified	

NSN 7540-01-280-5500

Standard Form 298 (Rev. 2-89)
Prescribed by ANSI Std. Z39-18
298-102